# Wind Tunnel Model Design for Sonic Boom Studies of Nozzle Jet Flows with Shock Interactions

Susan E. Cliff[1]
*Ames Research Center, Moffett Field, California, 94035*

Marie Denison[2], and Shayan Moini-Yekta[3]
*Science and Technology Corporation, Moffett Field, California, 94035*

Donald E. Morr[4]
*Millennium Engineering and Integration Services, Moffett Field, California, 94035*

Donald A. Durston[5]
*Ames Research Center, Moffett Field, California, 94035*

**NASA and the U.S. aerospace industry are performing studies of supersonic aircraft concepts with low sonic boom pressure signatures. The computational analyses of modern aircraft designs have matured to the point where there is confidence in the prediction of the pressure signature from the front of the vehicle, but uncertainty remains in the aft signatures due to boundary layer and nozzle exhaust jet effects. Wind tunnel testing without inlet and nozzle exhaust jet effects at lower Reynolds numbers than in-flight make it difficult to accurately assess the computational solutions of flight vehicles. A wind tunnel test in the NASA Ames 9- by 7-Foot Supersonic Wind Tunnel is planned for February 2016 to address the nozzle jet effects on sonic boom. The experiment will provide pressure signatures of test articles that replicate waveforms from aircraft wings, tails, and aft fuselage (deck) components after passing through cold nozzle jet plumes. The data will provide a variety of nozzle plume and shock interactions for comparison with computational results. A large number of high-fidelity numerical simulations of a variety of shock generators were evaluated to define a reduced collection of suitable test models. The computational results of the candidate wind tunnel test models as they evolved are summarized, and pre-test computations of the final designs are provided.**

## Nomenclature

| | | |
|---|---|---|
| $\Delta P/P$ | = | overpressure coefficient, $(P_L - P)/P$ |
| $C_p$ | = | pressure coefficient |
| $h$ | = | model altitude at model nose, inches |
| $L$ | = | model reference length, inches |
| $M$ | = | Mach number |
| $NPR$ | = | $P_{TN}/P$ |
| $P$ | = | free stream static pressure, psf |
| $P_L$ | = | local static (rail) pressure, psf |
| $P_{TN}$ | = | total pressure in nozzle plenum |
| $P_T$ | = | free stream total pressure, psf |
| $Re$ | = | Reynolds number, non-dimensional, $\rho VL/\mu$ |
| $X$ | = | longitudinal position, inches |
| $\alpha$ | = | angle of attack, degrees |
| $\phi$ | = | off-track or roll angle, degrees |

---

[1] Aerospace Engineer, Computational Aerosciences Branch, NASA Ames, AIAA Associate Fellow
[2] Research Engineer, Science and Technology Corp, Computational Aerosciences Branch, NASA Ames, AIAA member
[3] Research Engineer, Science and Technology Corp, Computational Aerosciences Branch, NASA Ames, AIAA member
[4] Research Engineer, Millennium Engineering and Data Integration Services, Experimental Aero-Physics Branch, NASA Ames
[5] Research Engineer, Experimental Aero-Physics Branch, NASA Ames, AIAA Senior member

## I. Introduction

The Commercial Supersonic Technology (CST) Project under NASA's Fundamental Aeronautics Program is developing technologies to enable future supersonic civilian aircraft to fly over land with reduced sonic boom. NASA's industry partners have developed designs excluding the effects of the nozzle plume and have recently begun including the inlet and nozzle flows in their sonic boom predictions (Ref. 1-6). Airframe shaping for quieter sonic booms has been largely successful, but there remains the challenging problem of predicting the sonic boom loudness with the complex flow field interactions between the jet exhaust nozzle plume and the shock waves generated by the surfaces at the aft end of the aircraft. In order to understand this complex flow field, the CST project has provided funding for the design and execution of a nozzle plume and shock interaction test in the NASA Ames 9- by 7-Foot Supersonic Wind Tunnel in February 2016. Rather than testing one of NASA's contractors' low-boom designs that includes nozzle jet flow, the goal was to design simple test articles to enable validation of the experimental data with computational methods for a wide variety of components, to replicate shock waves from various tail sizes and shapes, wing and aft-body components, as well as aft-deck shapes that shield upper surface mounted engines. The effects of the inlet and nozzle jet flows on the sonic boom performance of modern aircraft designs vary, and are dependent upon the size, position and shock strength of an aft-located shock generator as its shocks interact with the nozzle plume. The plume will be established in the wind tunnel test by blowing cold high-pressure air through an analytically-defined nozzle over a range of nozzle pressure ratios (*NPR*). Shock angle changes through the plume depend on the Mach number difference between the plume and the free-stream, and the Mach number in the plume is altered by variation of the nozzle pressure ratio.

An experiment in the 1- by 1-Foot Supersonic Wind Tunnel at NASA Glenn Research Center (GRC) was performed in 2014 where an isolated analytically-defined nozzle body (Ref. 7) was tested for a series of nozzle pressure ratios. A single static pressure probe traversed through the pressure field above and below the nozzle jet with shocks passed through the jet flow. The shocks were generated by an unswept double-wedge or aft-deck shock generators (Ref. 8). CFD computations were performed for various models and experimental flowfields with good results when the wind tunnel walls were included in the solutions (Refs. 9-12), but the close proximity of the walls of the tunnel restricted the range and altitudes of the sonic boom data.

The NASA Ames 9x7 Supersonic Wind Tunnel is one of the largest supersonic wind tunnel facilities in the United States (Ref. 13-14). The experiment in February 2016 is a follow-on test to the 1x1-foot test that will provide complete pressure signatures at significantly greater altitudes below and off-track the nozzle centerline for Mach numbers from 1.6 to 2.0. It is expected that measurements will be made of the complete model setup including the forebody shock, the nozzle exit shocks, the entire signatures of all shock generators (leading and trailing shocks) after passing through the plume, and some portion of the pressure field beyond the trailing edge shock of each shock generator. Larger reflection-free plume regions will be attained for the higher Mach numbers because of the fixed pressure rail height and Mach angle changes. The data from the test is expected to be of high quality, utilizing the recent developments in sonic boom testing from the N+2 studies (Refs. 15-16) and the use of averaged pressure signatures with the Reflection Factor 1 (RF1) pressure rail (Ref. 17). In addition to obtaining high-quality pressure signature data, a retroreflective focusing Schlieren (RFS) flow visualization technique (Refs 18-19) will be employed to provide images of density gradients in the tunnel.

CFD was used extensively to design a set of test articles for the planned experiment in the Ames 9x7 wind tunnel. The goal of the CFD studies was to develop knowledge of the flow field for notional configurations of interest and then define a reduced collection of test models worthy of testing. Analytic shapes were defined, grids generated, and solutions attained, for many different shock generator shapes. Navier-Stokes computations of the external flowfield as well as computational modeling of the internal nozzle were provided to assess various test articles shock strength, position, and changes through nozzle jet flows. Computations were used to study: forebody

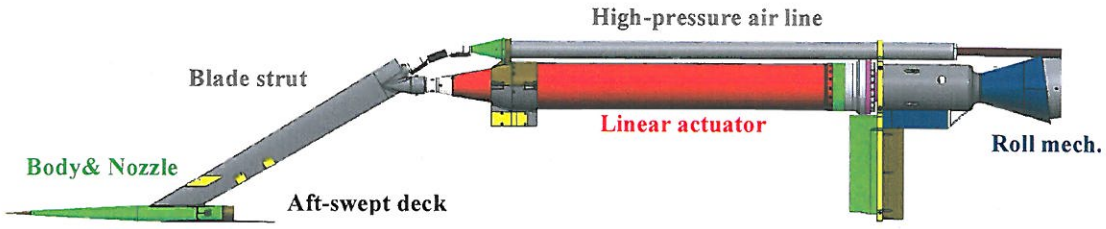


**Figure 1. Side view of final experimental set up.**

shape, nozzle size, small and large swept and unswept shock generators, and aft-deck shape. In addition, the main cantilevered blade strut that attaches the nozzle-body and shock generator components to the model support system was studied with CFD. Its sweep and shape at the joint where it attaches to the model support were preliminarily designed via assessment of the computational results. An image of the final design of the experimental set up is provided in Fig. 1. This is the aft-swept deck configuration with the deck attached below the aft-body and nozzle. The body, nozzle, deck, and blade-strut on the left side of the image are the components that were designed with CFD. High-pressure air is supplied to the body through the strut at its top and the entire model is supported at the bottom piece of the strut (white components). The linear actuator (red) is used to drive the ram (white) fore and aft for axial translation of the model. The gray component, aft of the linear actuator, is a 10-inch adaptor to place the model relative to the pressure rail for full signatures from Mach 1.6 to 2.0 and altitudes from 7 to 35 inches. The dark blue component is the roll mechanism to provide off-track experimental data.

## II. Experimental Facility, Instrumentation, and Operation Plans

The Ames 9- by 7-Foot Supersonic Wind Tunnel is part of the Unitary Plan Facility at NASA Ames Research Center. It is a continuous flow, closed circuit tunnel equipped with an asymmetric sliding-block nozzle for setting the tunnel test section free-stream Mach number. The floor of the wind tunnel test section is the movable part of the nozzle block. It translates axially (streamwise) to vary the throat area and provides a Mach number range of 1.55 to 2.55. The stream angle varies throughout the test section by approximately 0.25° to 0.5°, and it is greater in the vertical plane because of the asymmetric nozzle formed by the floor and ceiling. Models are positioned with wings vertical in the test section because of this stream angle bias, and therefore the angle of attack plane is horizontal.

The RF1 pressure rail (Ref. 17) mounts to the north sidewall of the test section and is used to measure the pressure signatures "below" the model. It has a 14-inch standoff distance of the pressure orifices from the tunnel wall that provides reflection-free data for a model up to 35 inches long at Mach 1.6, without contamination from shocks reflected from the wall. A layout of the aft-swept deck model assembly and RF1 rail in the wind tunnel is shown in Fig 2. Downward and reflected shocks from the model and wall are displayed with dashed line types. The distance from the model to the tip of the rail is controlled by the wind tunnel strut, shown as the vertical black line on the right side of the figure. The strut moves the model horizontally in the test section. The strut is located at the downstream end of the test section and its center body contains a mechanical joint to control the angle of attack of the model and associated mounting hardware. The center of rotation (CoR) is displayed as a red dot in the layout image. The strut is clipped in the image, but spans the walls of the tunnel. The roll mechanism (orange) to the right of a 10" adapter (green) is used to roll the entire cantilevered assembly for off-track pressure signature measurements.

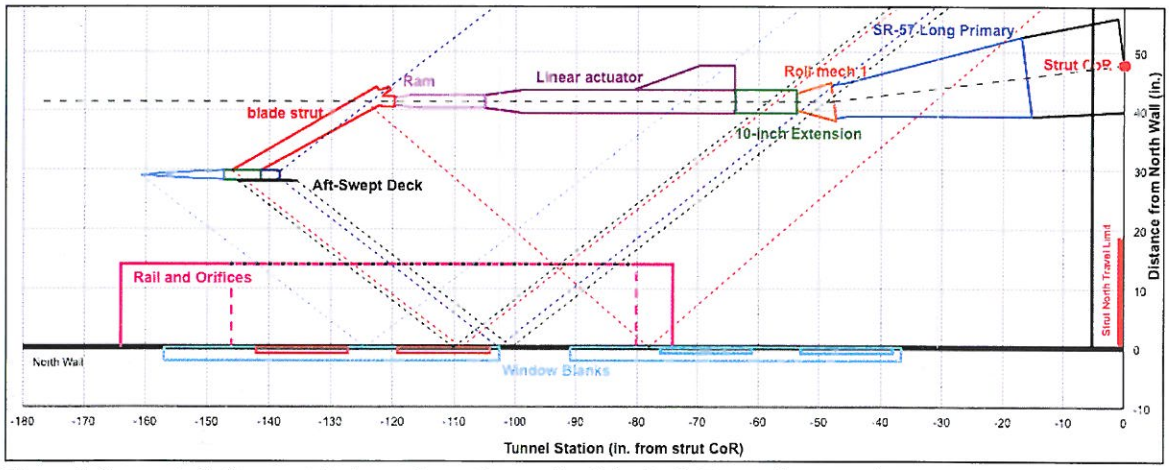


**Figure 2. Layout of aft-swept deck configuration and rail in the 9x7 tunnel test section.**

The tunnel can operate at total pressures between 634 and 3600 psf with corresponding Reynolds numbers between 0.5 and 5.7 million per foot. For sonic boom tests, the Mach number and total pressure are prescribed rather than the Reynolds number, and the tunnel is set at a $P_T$ of 2300 psf (slightly above atmospheric pressure). This provides a Reynolds number per foot of $4.4\times10^6$ in the tunnel test section at Mach 1.6.

## III. Computational Method

The unstructured module within the Launch Ascent and Vehicle Aerodynamics (*LAVA)* framework is used for all computations (Ref. 20). *LAVA* offers a variety of modules for robustly handling complex geometries or rapidly handling less complex geometries. The unstructured module that was employed here solves the compressible Navier-Stokes equations on unstructured arbitrary polyhedral meshes. A second-order accurate finite-volume discretization is implemented with flux computations at the cell center. The Spalart-Allmaras turbulence model was selected for most all computations. *LAVA* has been found to be robust and rapidly spreads the sonic boom pressure field within the domain with small number of iterations. It is a dimensional code requiring SI units and may take advantage of further improvements in IO to make it user friendly.

The grid generation techniques during model design differed from those for analysis. Design configurations were generated quickly by using a script for generating parameterized geometry with structured meshes using *Chimera Grid Tools* (*CGT*) software (Refs. 21-22) developed for overset methods to generate analytically defined surface meshes. These initial surface meshes were then used to generate unstructured polyhedral volume grids within a near-body cylindrical region utilizing a commercial software package called *StarCCM+* (Ref. 23). Subsequently, Mach-cone aligned hexahedral cells were appended to the cylindrical domain boundary in layers up to multiple body lengths away. The Mach-cone aligned hexahedral cells were generated with an in-house program that follows a method for accurate sonic boom analyses first introduced in 2011 (Ref. 24). The complete mesh was then used for computations with *LAVA*. This rapid method of obtaining computational results was applied to approximately 45 intermediate designs within a 4-month period of time. Although some mesh quality was traded for expedient meshing, the meshes used during design were suitable to identify pressure signature differences.

The symmetry plane and surface meshes of a Lockheed-Martin equivalent body of revolution with a free-floating shock generator (without strut) are shown in Fig. 3. The meshes used during the manual design studies varied, but this figure provides a good example of the quality of meshes generated during design. The volume mesh utilizes refinement regions around the plume and the small shock generator, and Mach cone aligned cells are used, but the

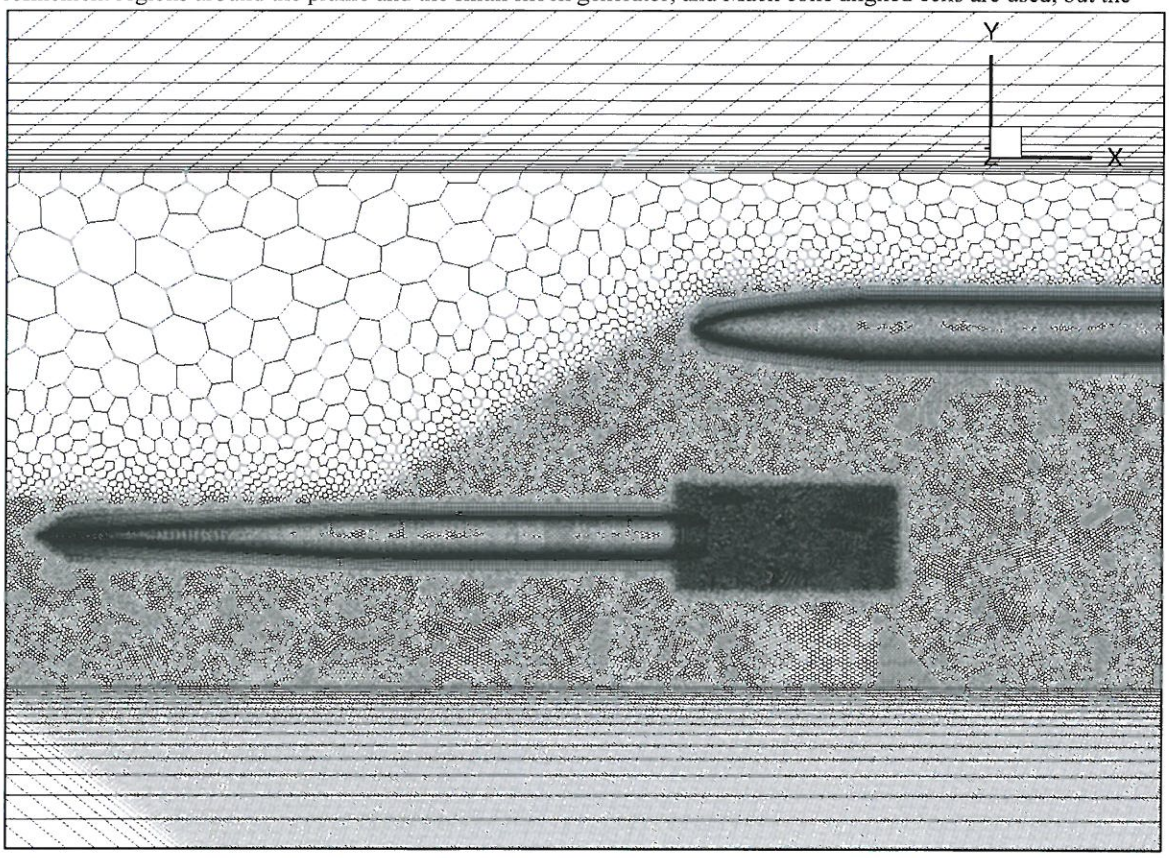


**a) Surface and symmetry plane**

**Figure 3. Example of design mesh (continues).**

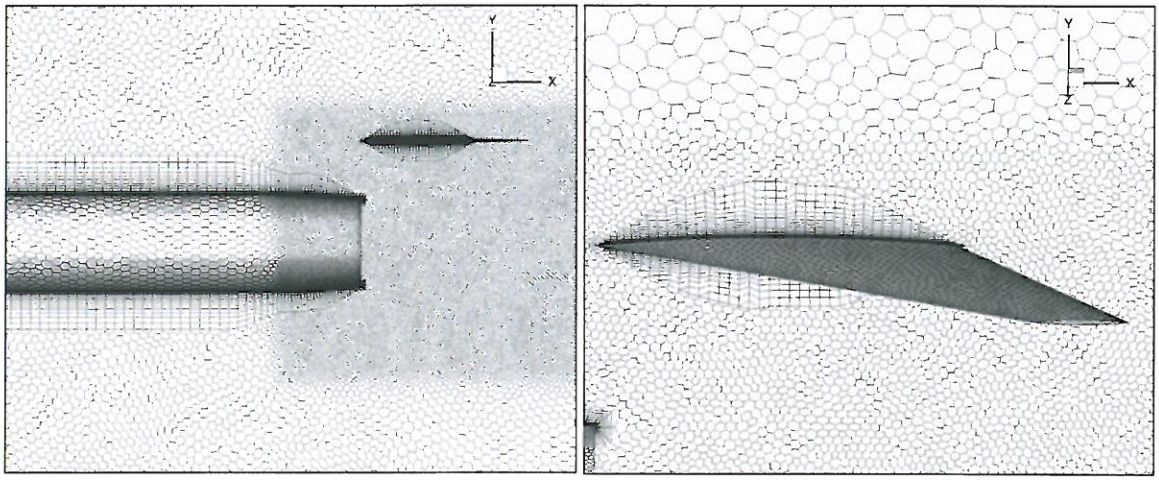

**b) Aft nozzle-body surface and symmetry plane** **c) Biconvex shock generator surface grid**

**Figure 3. Example of design mesh (concluded).**

resolution of the surface grids are coarser than a best practice mesh (later shown) would be. Figures 3(b and c) show that the surface mesh around the body and tip of the biconvex shock generator are coarser than desired for highly accurate pressure signatures. The cylinder that surrounds the test articles is slightly bigger than it needs to be and delays the initiation of the Mach aligned mesh. Minimizing the cylindrical mesh radius has been shown to reduce dissipation and improve the sharpness of shock waves.

Analyses of final design configurations at the test team's preliminary design review (PDR) and thereafter utilized best-practices gridding techniques for sonic boom computations (Ref. 25) with more refined meshes (26 to 49 million cells) than used for the design computations (10 to 20 million cells). High quality surface meshes of triangles and quadrilaterals were developed using a commercial software package called *ANSA* from Beta CAE Systems USA, Inc. (Ref. 26). Volume meshes were then generated with refinement regions within a minimally sized near-body cylinder, and a Mach-aligned collar grid was appended to the cylindrical mesh, as outlined above.

The difference in the solutions with the rapid design and the best-practice analysis meshing techniques was characterized by evaluating the forebody of the Lockheed equivalent body-of-revolution with both meshing techniques. The pressure signatures of the forebody, computed with both meshing strategies, are compared in Fig. 4. This comparison quantifies the errors in the design solutions. The design computations do not possess the same level of sharpness to the shock, but are of adequate accuracy for comparison of the design parameters studied herein. Note that the pre-test and final design CFD computations in later sections use the higher quality, analysis meshing methods. The Reynolds number for the design computations at Mach 1.6 were $4.4 \times 10^6$ per foot.

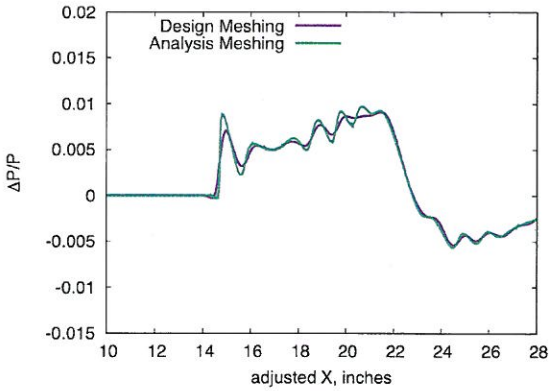


**Figure 4. Pressure signature comparison of design vs. analysis meshing techniques, LM equivalent body, $M$=1.6.**

## IV. Studies of Experimental Model Designs

Studies of fore-body shape, nozzle size, blade-strut sweep, nozzle pressure ratios, aft-deck size and plate bevel angles, and size and positions of shock generators (SG) were obtained. Nearly all of the parametric studies and the philosophies for the design choices are presented. Most of the designs varied two or more parameters at a time due to the very limited time available to develop a design. Limited model fabrication funds and testing time are available for this test, so to be cost effective the designs were kept simple and analytically defined so that a greater variety of configurations could be built and tested. The resulting designs from the studies presented herein should help industry assess models with horizontal tails of various sizes, and aft-deck configurations with upper surface mounted engines and with forward- or aft-swept trailing edges. In the next sections, details of the intermediate designs are presented.

### A. Fore-body Shape and Strut Sweep

Ideally, an experiment would have inlets and nozzles that would simulate the propulsive flows as on a real airplane, with the nozzle exit air at the correct NPR and temperature. However, the small scale of the subject model precludes the accurate simulation of the inlet and nozzle flows, and so for the purposes of measuring plume/shock interactions, no inlet flows are simulated, and the nozzle flow is simulated with cold high-pressure air pumped to the model through the wind tunnel strut. None of the usual airplane components are modeled for this test except for the various shock generators representing horizontal tails placed above the nozzle and the aft decks placed underneath the nozzle. The "fuselage" of this model is simply a body of revolution terminating with a single nozzle.

An equivalent body of revolution representing a modern low sonic boom vehicle with an enclosed aft nozzle was initially used to provide relevant (low overpressures and shaping) pressure signatures. A similar body of revolution was run in recent sonic boom tests in the 9x7 wind tunnel (Ref. 15), and provided a good representation of a complete vehicle's sonic boom pressure signature. For the upcoming test, the Lockheed-Martin Aeronautics Company (LM) provided the equivalent body shape corresponding to one of their business-jet sized low-boom study vehicles. Its aft region is cylindrical which allows the Putnam nozzle 6 (Ref. 7) previously tested in the 1x1-foot wind tunnel at GRC to be incorporated into the aft cylinder section.

The first computational study modeled the aforementioned LM business-jet equivalent-body with a 1-inch Putnam nozzle 6 at a *NPR* of 14, along with a free-floating swept "tail" shock generator (SG) above and aft of the nozzle. A parabolic-nosed body was used initially to represent the upstream end of the model supporting hardware. This configuration was also evaluated with two possible struts, with sweep angles of 55° and 65°. Figure 5 shows isometric views of these three computational models with a red arrow that points to the small SG. The swept struts attach the nozzle body and SG to the model support and provide for high-pressure air routing to a nozzle plenum. These initial struts were simply defined with double-wedge cross section (easily defined analytically) and the free-stream chord was 3.12 inches with t/c of 7.0-percent. The shock generator shape was loosely taken from the tail from the Ames Low Boom Wing Tail design from 1993 (Ref. 27). It was used because it possessed typical sweep, thickness, and taper and was sized for takeoff and landing during the referenced paper-studies in the 1993. The initial SG was very small with 5%-thick parabolic biconvex sections and a root chord of 1.18 inches.

**a) Without strut** **b) With 60° swept strut** **c) With 65° swept strut**

**Figure 5. Isometric views of initial geometry setups with Lockheed Martin equivalent body of revolution.**

Figure 6 shows contours of density gradient magnitudes on the symmetry plane and overlays the pressure signature 15 inches below the nozzle centerline; the pressure signature is presented at only one altitude to clearly allow the reader to trace along the shock lines to the origin of pressure change on the model. No axes are provided on the images since the pressure signatures are plotted with axes in subsequent plots throughout the report. A gray-scale contour legend is shown in Fig. 6a. The same range of contour levels was used for all figures, thus legends are not provided in subsequent figures. The strut sweep changes in the latter two subfigures (b and c) are very subtle but are somewhat apparent in the difference in magnitude of the shock from the intersection of the lower part of the strut with the nozzle body (shock peak immediately after the first negative-pressure region).

In the N+2 winged-vehicle wind tunnel model designs (Ref. 15-16), the shocks from the model struts were shielded by the wing and were of such small magnitudes that the strut did not affect the on-track pressure signatures. Note that the struts from the N+2 studies were swept at about 75° and 73° relative to free-stream during the N+2 Phase I and II experiments of Lockheed configurations, respectively. Hence with the current plume/shock interaction model having no wing to shield the strut, the initial choice for strut sweep was 65° since it yielded the smaller pressure disturbance in the flow, and this sweep angle was less than previously tested during the N+2 studies which would reduce the likelihood of flow separation on the strut.

The magnitude of the density gradient shown in this figure is similar but different to what should be visible with the Schlieren images that shows the density changes in the wind tunnel within a finite spatial region in the flow field (Ref. 18). This function was selected because it provides visualization of computed shock and expansion waves at

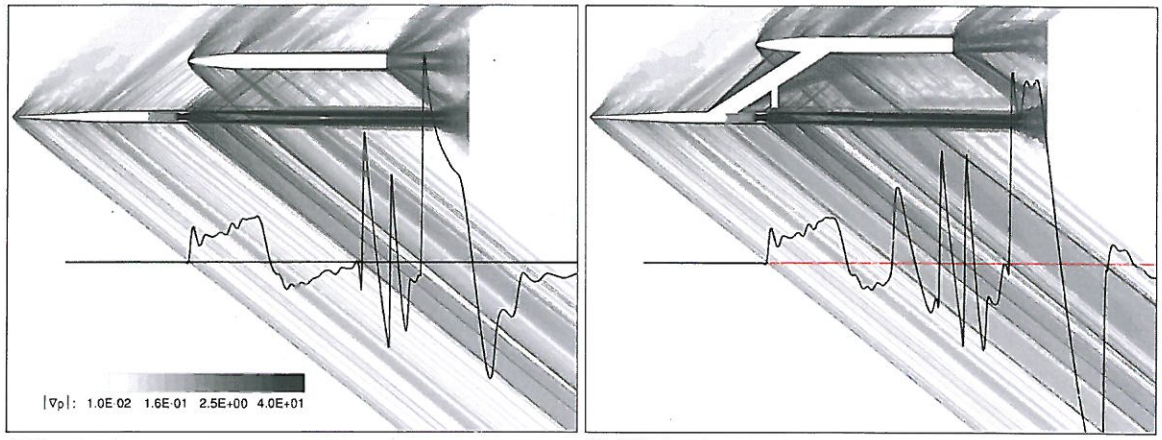


a) No strut

b) 60° strut

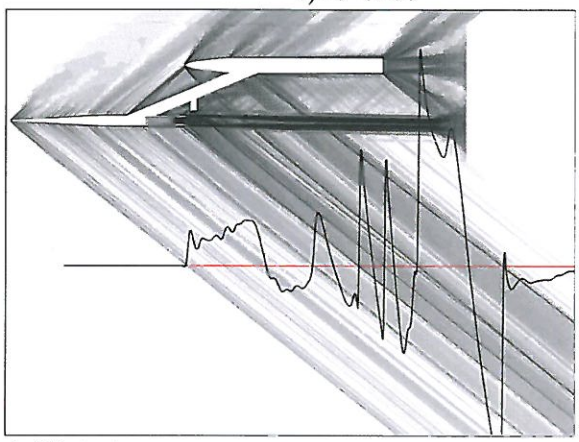

c) 65° strut

**Figure 6. Pressure signatures at $h$=15 inches over contours of density gradient magnitude of LM equivalent body with different strut sweeps, $M$=1.6, $NPR$=14.**

significantly larger distances from the model than contours of $Cp$ or Mach number, for example.

Figure 7 overlays the pressure signatures of the three models. The forward portion of the pressure signature represents overpressures of a present-day low-boom configuration and provides a basis to compare the pressure signature of the forth-coming series of SG's against. The pressure signatures from the LM equivalent body are shown for the model without a strut for $X$ < 32 inches. The relative shock strengths of the struts swept at 55° and 65° can now be easily compared with each other at $X$=28 inches, and to the equivalent-body signature (14 < $X$ < 27 inches). This reveals that the 60° strut shock is stronger than the overpressure of the LM body and that the 65° swept strut reduces the strut shock from 0.015 to 0.01.

The shock at $X$=33 inches appears to be from the lower edge of the nozzle lip, and the SG leading shock has coalesced with the lower nozzle shock at $X$=36 inches. The trailing shock from the small SGs is difficult to place and may have coalesced with the sting shocks at $X$=38-40 inches.

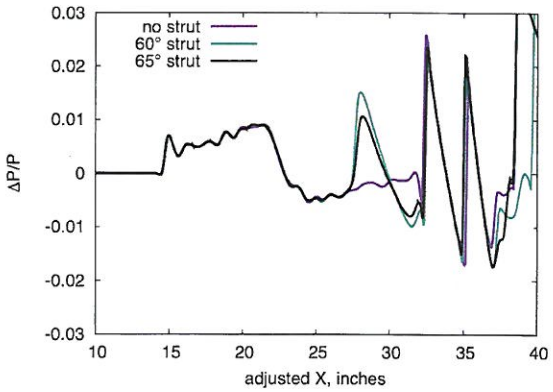


**Figure 7. Effect of strut sweep with the Lockheed-Martin equivalent body.**

### B. Nozzle-Body Size and Integrating the Strut with the Sting

The next design analyses were used to evaluate an increase in nozzle size to make use of the larger tunnel size (the 9x7 relative to the 1x1) and provide more detailed pressure signatures of the nozzle exit and plume shocks. Initially, the outer diameter of the Putnam nozzle 6 used in the 1x1 test was doubled to 2 inches, and at the same time the junction between the top of the swept strut and the model supporting hardware (referred to as the sting) were blended together, essentially eliminating the bow shock from the parabolic nose of the sting. Thus, the top of the strut was modified to bend from 65 degrees back to free-stream while growing the thickness to meld with the model-supporting sting. The first design of a blade strut concept with a similar integration of the strut with the sting is attributed to Gulfstream (Ref. 28). The transition between the strut and sting in this design was done in a crude fashion (without CAD methods) in these preliminary studies.

Growing the nozzle body to 2 inches seemed like a small change, but it quadruples the area of the nozzle and requires the length of the model to double, making the model very large for sonic boom testing. To reduce the overall model length after scaling, the nozzle plenum was inserted deeper into the 2-inch diameter part. For the 1-inch nozzle-body, the nozzle plenum boundary was 6.62 inches from the start of the cylindrical portion of the body, and for the 2-inch nozzle it was 2.79 inches from this point, resulting in overall lengths of 23.01 and 29.13 inches for the 1- and 2-inch nozzle bodies, respectively. However, the 2-inch diameter model was still too big to obtain complete signatures for the range of desired altitudes ($7 < h < 35$ inches) with the RF1 pressure rail, and the added stress to the cantilevered model support system may have been problematic, so the model diameter was selected to be 1.5 inches. This size nozzle would allow for similar model lengths to those tested in the N+2 studies and would allow for reflection-free signatures of the nozzle-body and attached shock generators at Mach 1.6.

Figure 8 allows for the comparison of the 1- and 2-inch nozzle bodies' density gradient contours on the symmetry plane with overlaid pressure signatures at 15 inches for Mach 1.6, and *NPR* 14. The signatures are overlaid in Fig. 9; the 2-inch diameter model shows greater detail, as expected, but some of the differences are also due to lower mesh resolution for the 1-inch model. The forebody nose-to-cylindrical portions of the pressure signatures are to $X$=23 and 30 inches for the 1- and 2-inch bodies, respectively.

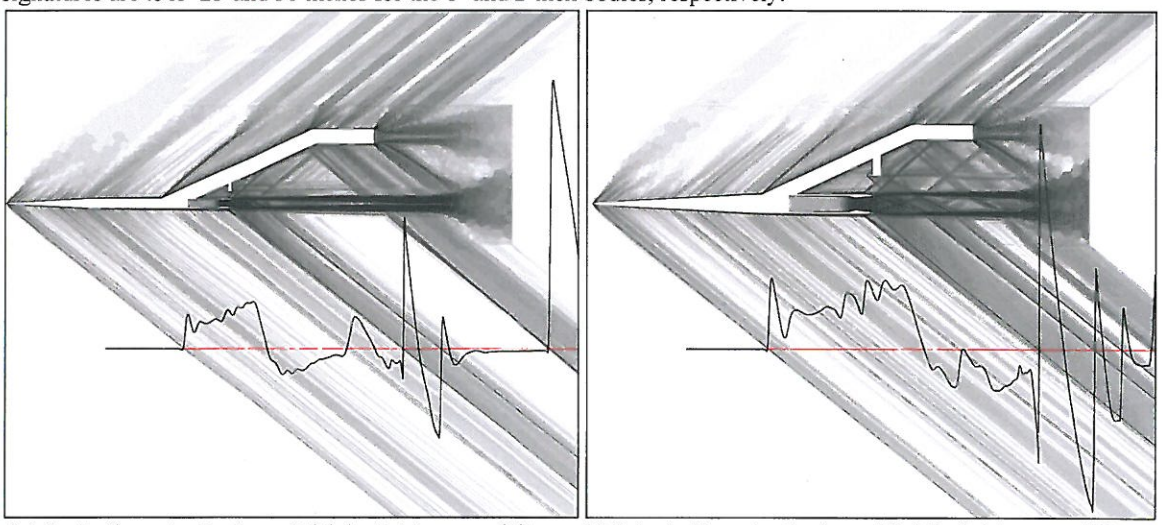

**a) 1-inch diameter body and 1.0-inch biconvex SG** **b) 2-inch diameter body and 2.0-inch biconvex SG**

**Figure 8. Pressure signatures at $h$=15 inches over contours of density gradient magnitude for different sized nozzle bodies with the LM equivalent area definitions.**

The effect of integrating the strut with the sting is shown in Fig. 10. The "sting shock" in the integral strut-sting appears at $X$=52 inches, whereas the shock from the individual sting appears much closer to the SG signature at $X$=38 inches. Having a large distance from the trailing shock of the SG to the sting shock is important for analyses of the plume region as the SG shock returns to ambient flow amidst the influence of the nozzle jet stream. Thus, the integral sting (as-designed) is superior. The separate sting design could have had a smaller length nose, but would result in a blunter nose shape with an associated stronger shock.

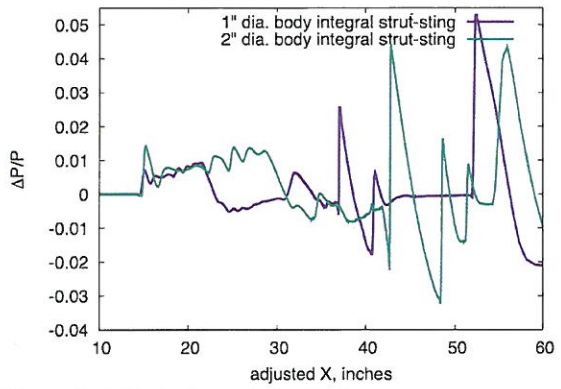


**Figure 9. Effect of nozzle-body size.**

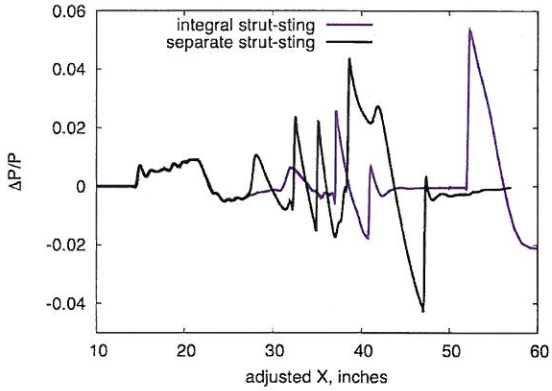


**Figure 10. Effect of integrating the strut and sting (1-inch dia. body).**

### C. Forebody Simplification

The LM forebody was deemed unnecessary for the studies of nozzle plume and shock interactions because the complexities of the forebody signature were inconsequential to the plume-shock interactions downstream and manufacturing a simpler model would avoid any difficulties or added expense to fabricate a body with very rapid changes in curvature over short distances. An analytic forebody shape was therefore selected with similar overpressures to the LM body. It was selected from experimental sonic boom data of a series of analytically-defined shapes by Carlson (Ref. 29). Carlson refers to the shape chosen for this model as "Model 6" in the 1965 report, and it was selected since it has low overpressures like the LM configuration. Carlson had selected this model shape from an earlier paper (1962) on design methods to attain low sonic boom overpressures (Ref. 30) because it achieved better low-boom characteristics than other models in the study.

The Carlson model 6 function described in the 1965 report had to be scaled in both vertical and axial directions so that it was 1.5 inches in diameter and stretched to an appropriate length. Axial stretching affects the bluntness of the model, so the scale chosen provided in a good match to the drawing of the model in the report. The method to scale the curve of the Carlson forebody is as follows:

1) Create curve using

$$y(x) = x\sqrt{\left(\frac{0.025}{\pi}\right)(1.0 - 0.3x)} \quad \text{for } x = [-5.24184, 0]$$

2) Scale coordinates

$x' = x * 2.53601862739$

$y' = y$

3) Translate to desired position

This results in a forebody-defining curve that is 13.29 inches long. A 1.5-inch cylindrical body follows this until the boat-tail angle from the Putnam nozzle is encountered, for an overall length of 23.01 inches. The forebody lengths for the 1-inch LM, 2-inch LM and 1.5-inch Carlson bodies are: 9.34, 18.32, and 13.29 inches, respectively.

The pressure signatures for the Carlson Model 6 body are overlaid with the 1- and 2-inch LM equivalent bodies in Fig. 11 at Mach 1.6, and *NPR* 14. The maximum overpressure for the Carlson body lies between the 1- and 2-inch equivalent bodies and therefore also represents overpressures of relevant vehicle designs. The Carlson nose shape results in a smooth rounded pressure signature. The experimental data in Carlson's report has the same characteristics as these computational results.

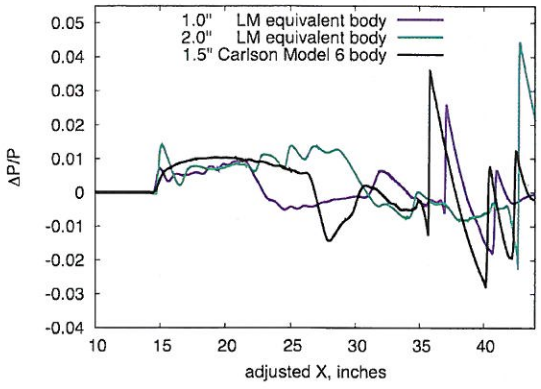


**Figure 11. Comparison of Carlson analytic forebody to LM equivalent body.**

### D. Whole configuration pitch rotation versus SG incidence

The biconvex shock generator shape, derived from the tail of the Ames LBWT design from 1993 (Ref. 26), was sized to 1.5 inches at the root chord and retained the sweep of 58° and taper of 0.351 from the earlier design. Figure 12 shows isometric, side and top views of the test rig with the 1.5 inch biconvex SG. A black arrow points to the small SG in Fig. 12a.

**a) isometric** **b) side** **c) top**

**Figure 12. Images of the surfaces of the biconvex shock generator setup.**

The SG design sought would have a shock strength that was large enough to be experimentally assessed, yet small enough that it was not more than 2-3 times that of its' forebody (representative of contemporary low boom designs). Recall that the Carlson forebody and cylinder overpressures are suitable to compare to without requiring the manufacture of the LM equivalent body.

Figure 13a shows the density contours of the biconvex SG through the jet flow at a *NPR* of 8.0 and a Mach number of 1.6. The symmetry plane density gradient contours show the position of the shock generator in relationship to the shocks from the other model parts. The SG was placed so that the upward-directed shocks from the upper nozzle lip pass behind the trailing edge of the SG, and the downward-directed shock is upstream of the SG's bow shock. A short study was done to double the size of the shock generator to a 3-inch root chord, but the larger shock generator could not be positioned without the nozzle exit shock striking the SG (study not presented). Thus, the 1.5-inch root chord shock generator is the first concept selected for testing (geometry shown in Fig. 12).

The effects of changing the incidence angle of the biconvex SG from 0° to 2° and 4° was next studied. The density gradient contours with the biconvex SG at 0° and 4° are shown in Fig. 13. The nozzle plume changes the angles of the leading- and trailing-edge shocks from the biconvex SG as they pass through the plume at this *NPR*. Later in this paper, a study will show how *NPR* can severely affect the angle change of the shocks passing through the plume. Comparing the 0° and 4° solutions, the bow shock with the pitched SG has a stronger leading edge shock, and a hyperbolic shaped disturbance from the tip of the SG (approximately 1 chord downstream) is more prominent for the pitched model. Another detail of the design is that the size and placement of the downward strut (attaching

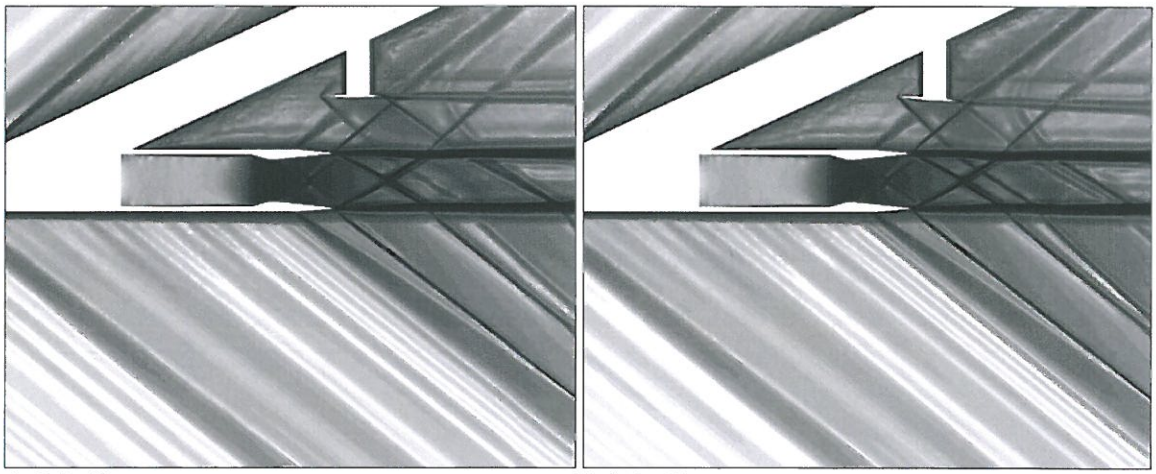

**a) alpha 0°** **b) alpha 4°**

**Figure 13. Density contours of the biconvex shock generator, $M$=1.6, $NPR$=8.**

biconvex SG to main strut), were such that the shocks from the leading and trailing edges would be fairly well shielded with the swept biconvex SG. Since the leading edge of the biconvex SG is swept at a greater angle (58°) than the trailing edge (29.2°), and this angle is greater than the Mach angle, the 0.75-inch downward strut was placed 0.524 inches from the leading edge and 0.224 inches from the trailing edge on the centerline of the biconvex SG for shielding. However, this downward strut was not retained in the final CAD design.

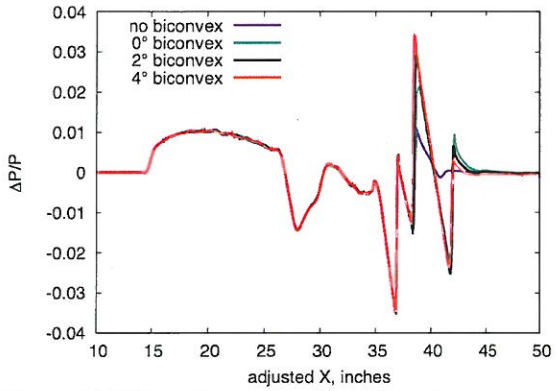


**Figure 14. Effect of at angle of attack and presence of the biconvex shock generator.**

The pressure signatures of the shock generator at 0°, 2° and 4° and without the shock generator (all at *NPR* of 8 and Mach 1.6) are overlaid in Fig. 14. The biconvex SG pressure signatures have an N-wave pressure distribution just upstream of the point before the flow returns to ambient pressure ($37.5 < X < 42.5$). The bow shock of the biconvex has coalesced with the shock from the nozzle upper lip (evident in the detailed images near the nozzle exit of Fig. 13 and the zoomed-out image of Fig. 15b that includes the pressure signature at 15 inches) and together they have a combined shock strength of $\Delta p/p = 0.02$. Without the SG in place the nozzle lip shock has about half that strength ($\Delta p/p$ of 0.01), so the shock strength approximately equal to the overpressures from the forebody (around $X$ =20) at zero degrees angle of attack. At 4° angle of attack the combined SG/nozzle lip shock has a $\Delta p/p$ of 0.035.

A pair of computations were preformed with the full model assembly rotated 4° in angle of attack, with just the biconvex shock generator pitched up 4° with the rest of the model at zero angle of attack. The purpose of doing these computations was to aid in deciding whether to fabricate two biconvex SGs (integral with their support struts, which fix their pitch angles) in order to learn the effects of this SG being inclined 4° to the freestream flow—the thought being that a full-model rotation could be sufficient to discern these effects. Obviously, not having to make two such pieces saves on design and fabrication time, as well as tunnel time and cost.

The contours of density gradient magnitude with full assembly rotation (Fig. 15a) show that the flow out the nozzle remains along the axis of the nozzle, with only the appearance of some small deflection where the mesh is coarse. The plume region is compared with the geometry fixed at 0° with the biconvex rotated in pitch 4° (Fig. 15b). Note that the mesh was refined in the plume region in Fig. 15a to understand the plume angle when pitched, but the mesh in Fig. 15b was not refined in the plume region much beyond the trailing edge shock of the SG.

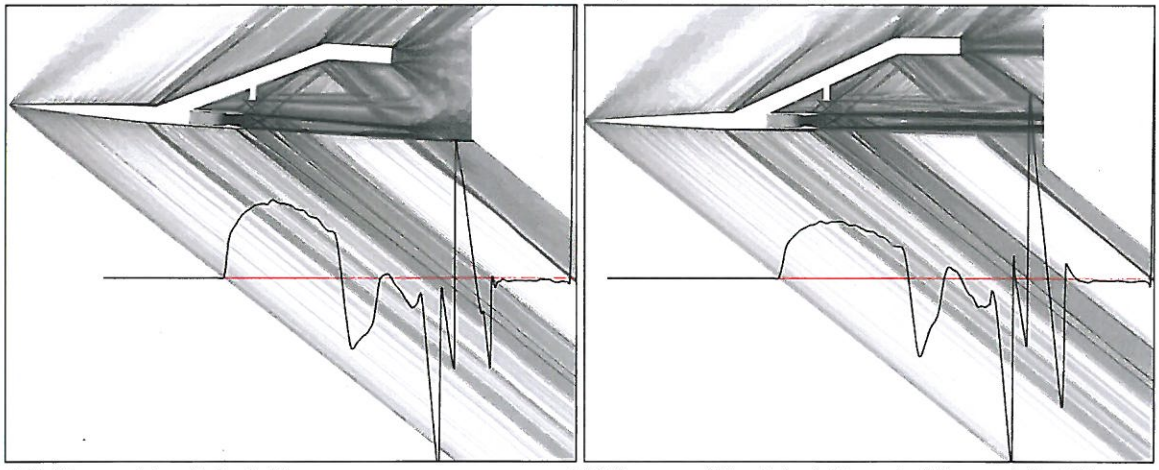

**a) Full assembly pitched 4°** **b) Biconvex SG pitched 4°, rest of the model at 0°**

**Figure 15. Pressure signatures at $h$=15 inches over contours of density gradient magnitude of LM equivalent body with different geometric rotations.**

Figure 16 quantifies the differences in the signatures. Some differences are due to vehicle rotation angle change which gives rise to different length pressure signatures. However, there is also a difference in shock strengths. The solution with full assembly rotation shows that the strength of the bow and tail shocks from the shock generator have not increased to the extent of the independently pitched shock generator. Although there are these differences in the pressure signatures, in the upcoming experiment only full-geometry rotations shall be employed. It was originally planned to test the rotated shock generator, but in order to reduce expenses and have enough time to test higher priority test articles, the 4° biconvex shock generator was eliminated.

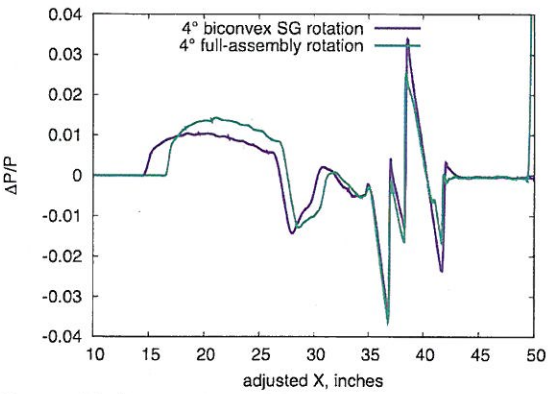


**Figure 16. Comparison of full assembly pitch rotation vs. SG pitch**

### E. Effect of Nozzle Pressure Ratio

The Putnam nozzle used in this study is a convergent-divergent nozzle that expands after the convergent region at a half angle of 6.04° and has an expansion area ratio of 1.72 which produces an optimal expansion *NPR* of 8.12 at a design Mach number of 2.02. The exterior nozzle boat tail angle is 5°. A cross section of the planned experimental nozzle-body and strut shows the internal flow path in Figure 17. The computational model imposed a boundary condition to the forward faces of a plenum region to control the *NPR*. The total pressure was prescribed to the desired nozzle pressure ratio times the free stream static pressure.

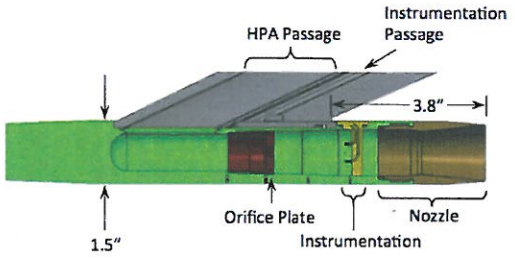


**Figure 17. Internal flow path through nozzle.**

A series of 6 computations were performed for *NPR*s from 4 to 14, for the test configuration with the 1.5-inch chord shock generator at Mach 1.6. Figures 18 and 19 show the pressure density gradient simulated at the different *NPR*s. Figure 17 shows the density contours for the whole assembly with overlaid pressures signatures at an altitude of 15 inches. Note the significant differences in the aft pressure signatures for the series of solutions. Not only are there shock strength differences there are shock location differences. Figure 19 shows an enlarged view of the region where the shock generator and nozzle plumes interact. The series of images show that the angle of the nozzle exit shocks and the angle from the shock generator change as they pass through the plume region. The shock angle changes as it passes through the plume because of the Mach number inside the nozzle plume, which is dictated by the *NPR*. This phenomenon was also revealed in the 1x1 tunnel experimental data as well as the computational simulations of models that include the wind tunnel walls (Refs. 8-12). The figure also shows that the shock angles changes in the plume region become more significant with increased *NPR*. For *NPR*s of 6 and 8 the shocks do not appear to change slope as they pass through the plume.

Figures 18 and 19 demonstrate the importance of knowing the engine *NPR* for accurate sonic boom analyses of flight vehicle concepts as well as any engine exit shape changes that might occur during flight operations. The pressure signatures of the computations with differing *NPR*s are overlaid in Fig. 20. The bow shock of the shock generator has moved aft from an *X* location of 37.5 to 40.1, and the shock strength has weakened by changing the *NPR* from 4 to 14. Whereas, the nozzle exit shock has moved forward from 37.5 to 36.0 inches, and strengthened. Shock position and strength changes of this magnitude could significantly affect a flight vehicles ground pressure signature.

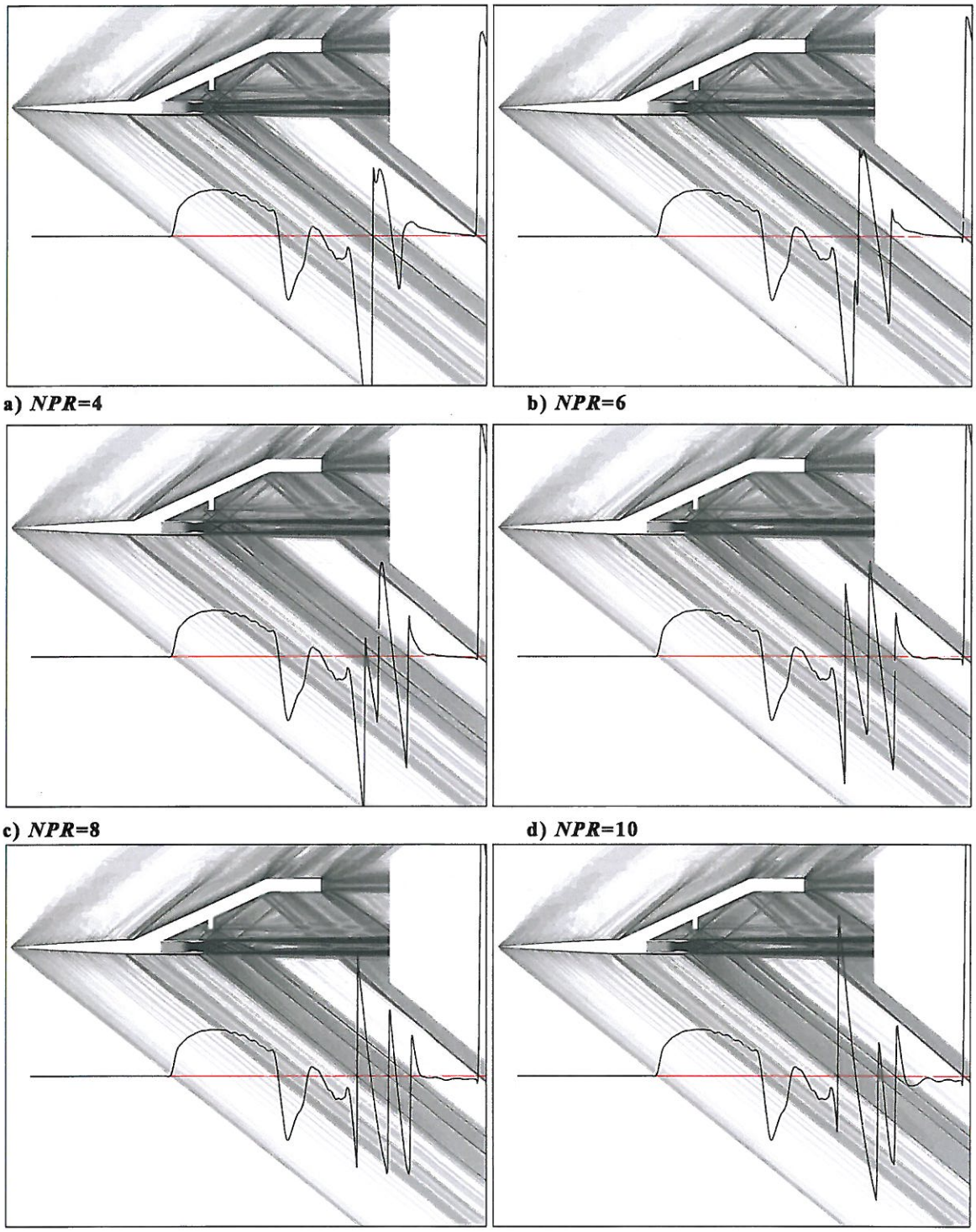

**a) *NPR*=4** **b) *NPR*=6**

**c) *NPR*=8** **d) *NPR*=10**

**e) *NPR*=12** **f) *NPR*=14**

**Figure 18. Effect of *NPR* on density contours and pressure signature at $h$=15 inches, $M$=1.6.**

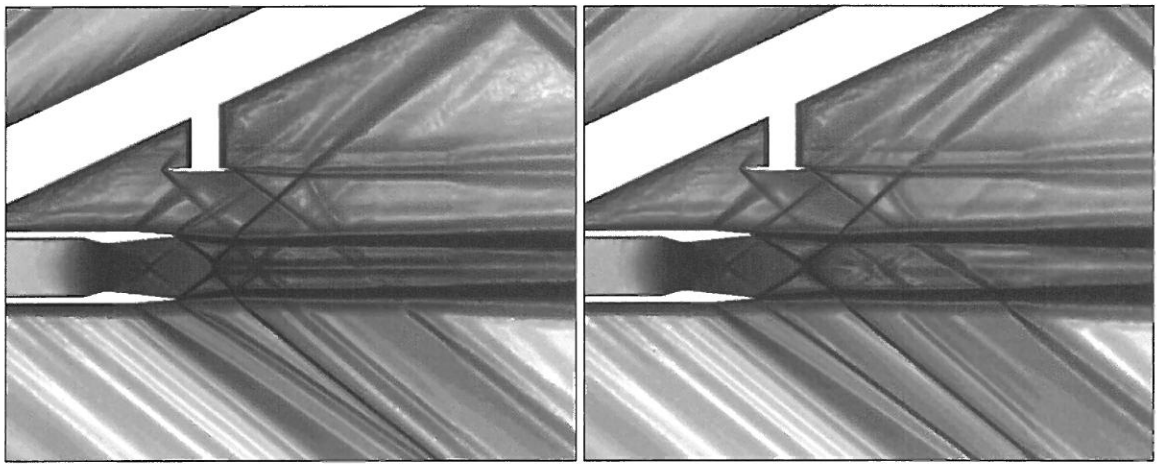

a) ***NPR*=4** b) ***NPR*=6**

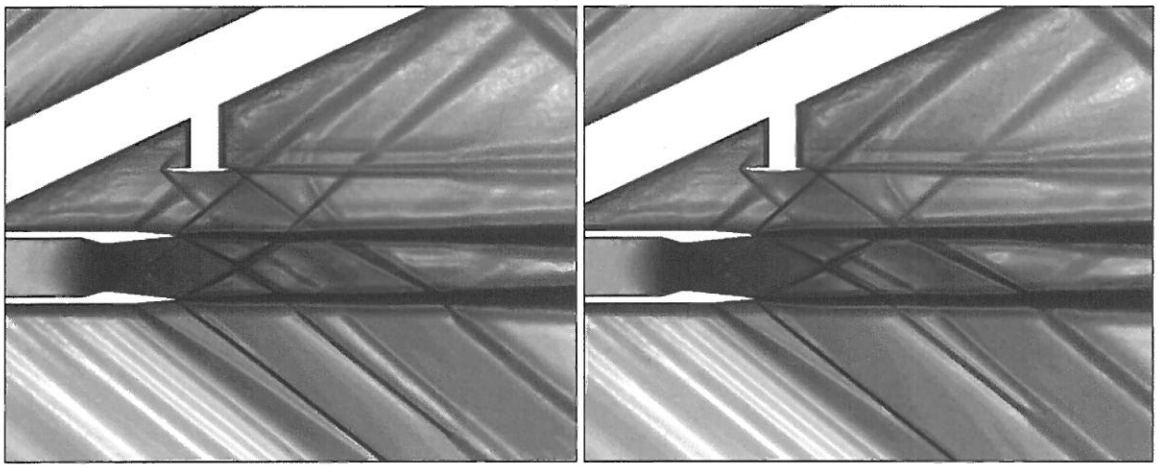

c) ***NPR*=8** d) ***NPR*=10**

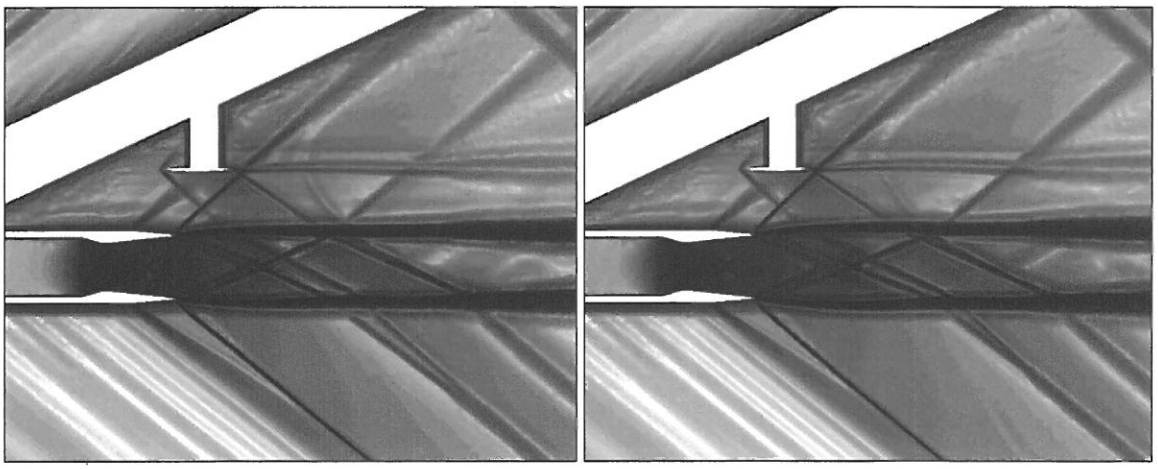

e) ***NPR*=12** f) ***NPR*=14**

**Figure 19. Effect of *NPR* on density contours in plume region, *M*=1.6.**

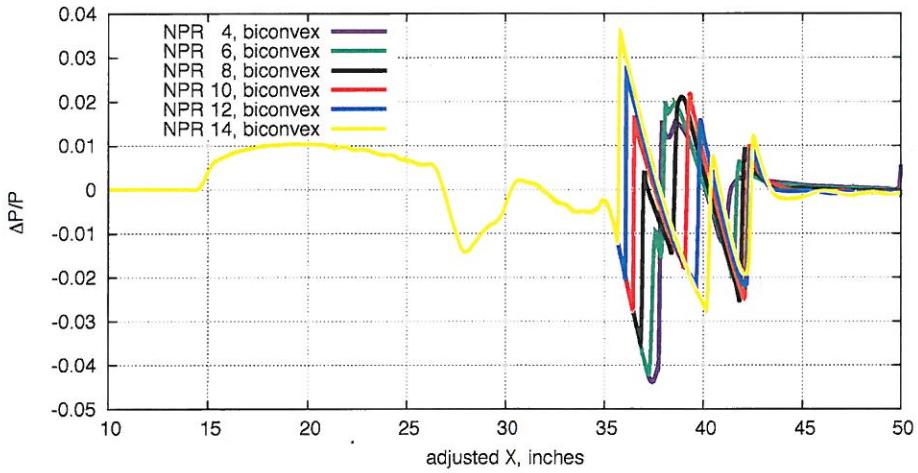


**Figure 20. Effect of *NPR* on pressure signature at *h*=15 inches.**

### F. Aft Deck Tip Bevel Angle

A flat plate of 0.125" thickness will serve as an "aft deck" to simulate aircraft designs where an engine would be placed on the upper surface of the deck so that inlet and nozzle exit shocks are shielded. Planform designs that encompassed both a trailing edge that extended 2- and 1-nozzle diameters aft of the nozzle exit were studied. Hereafter, these will be referred to as the "2-diameter aft deck" and "1-diameter aft deck". Figure 21 provides an image of the 2-diameter aft deck that has leading and trailing edges with 5° bevel angles, and the tip with a 15° bevel angle.

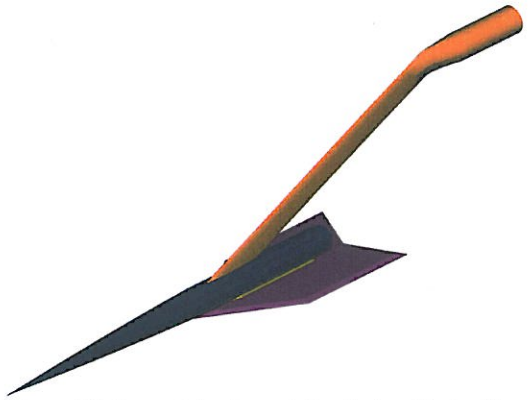

**Figure 21. Isometric view of the deck with trailing edge 2 nozzle diameters from the nozzle exit.**

Originally it was envisioned that two aft-swept decks would be required (without consideration of the *NPR* effects). Whereby the 2-diameter length to the trailing edge deck would shield the nozzle exit shocks and the 1 diameter length would not. The 2-diameter deck was computed with CFD first, since it is the better model for nozzle plume shock shielding and would likely offer a lower boom concept. A 15° bevel angle was initially used around all of the outer deck edges. Material is cut away from only the upper surface of the flat plate deck so that the shocks from the beveled surface reflect upwards and result in minimal shocks below the model from the deck edges. A study (not shown) indicated that the leading and trailing bevel angles had little affect on the signatures below the model. However, a 5-degree bevel angle was chosen for the leading and trailing edges to reduce the likelihood of flow separation from these edges and to reduce the strength of the upward shocks. Note that a small 3/32 inch height boundary layer diverter (0.7 inch width) was used to help attach the nacelle to the plate and to raise the nozzle to keep it out of the boundary layer, like an engine may be raised up if it had an inlet to prevent ingestion of the stagnate flow in the boundary layer. The decks were large enough that its leading edge would shield the strut leading edge shocks and the trailing edge at the centerline extended either 1- or 2- nozzle diameters aft of the nozzle exit, with equivalent semi-spans of 2-nozzle diameters.

A study of the tip angle was performed on the 2-diameter deck. Computations with tip bevel angles of 5°, 10°, 15°, 20° and 90° and a solution without a deck are compared in Fig 22. The deck shields the nozzle shocks between $X$ of 37 and 39 inches and the tip bevel angle has a fairly significant effect on the pressure signatures. The 5° bevel angle resulted in the weakest shock at $X$=32 inches and the 90° (blunt) tip had the strongest shock. The tip bevel angle also affects the aft pressures ($X > 34$). In this region, the 5° bevel has the strongest shock at around $X$=40, and the 90° bevel tip has the largest expansions and shocks. The 15° bevel tip results in the most benign pressure signatures, and hence was chosen as the tip angle to be manufactured.

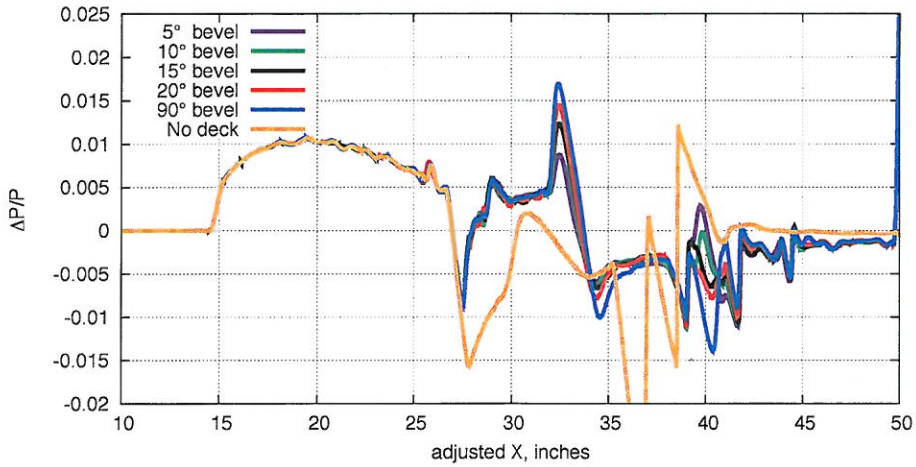


**Figure 22. Effect of deck tip bevel angle for the 2-diameter aft deck.**

Density contours for solutions with 5°, 15° and 90° tip angles are shown in Fig. 23. The non-linear waves that emanate below the deck, just aft of the decks' midchord, indicate pressure changes from an off centerline source. If the Mach cone from this source were a conical section sliced on the symmetry plane it would be hyperbolic in shape. Note that these non-linear waves are fairly pronounced here, and much more so for the deck with blunt tip (90° bevel angle in Fig. 23c.

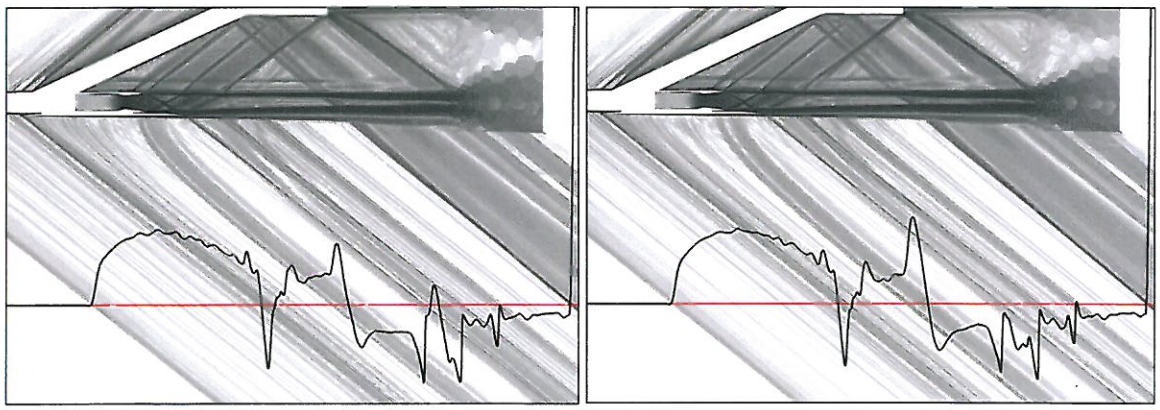

**a) 5° tip bevel** **b) 15° tip bevel**

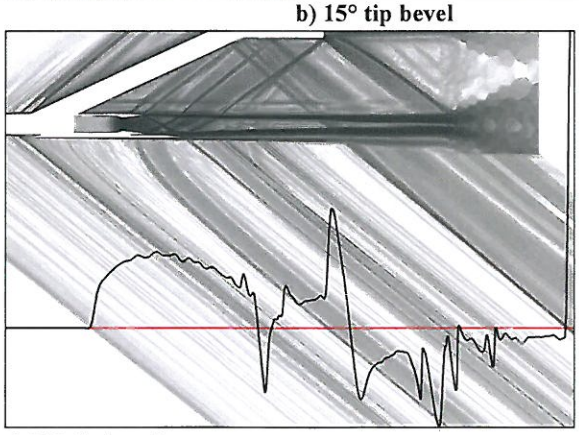

**c) 90° tip bevel**

**Figure 23. Density contours of the 2-diameter aft deck with different tip bevel angles.**

Investigations of the surface pressure coefficients also help explain the aft-deck pressure signature changes due to tip bevel angle differences. Figure 24 shows the design with 15° tip bevel angle and how the upper deck surface shields the nozzle exit pressures. Note that the range of the pressure coefficient contours displayed on part (b) of the figure is an order of magnitude smaller than shown in part (a). The deck shields both shocks from the nozzle exit lip as well as the expansion region from the nozzle boat-tail angle (Fig. 24a). The nozzle exit lip shocks appear in the first compression region behind the nozzle and an indication of another weaker compression region from the top of nozzle appears very near the aft trailing edge bevel. The aft-swept trailing edge concept was chosen for greater shielding than an un-swept or forward swept trailing edge since the sweep is the direction of the Mach cone angle. The shock from the blade strut is also shielded from the on-track pressure signatures, but the very small semi-span in this region may not be sufficient to limit the three-dimensional effects. Making the deck any larger would likely not satisfy the structural load requirements with the current blade strut design. The lower surface of the deck (Fig. 24b) reveals an "X" shaped compression pattern from the wing tip shocks, and results in a pressure spike where they merge at the symmetry plane. This is the spike in the pressure signatures at $X$=32 inches shown in Fig. 22.

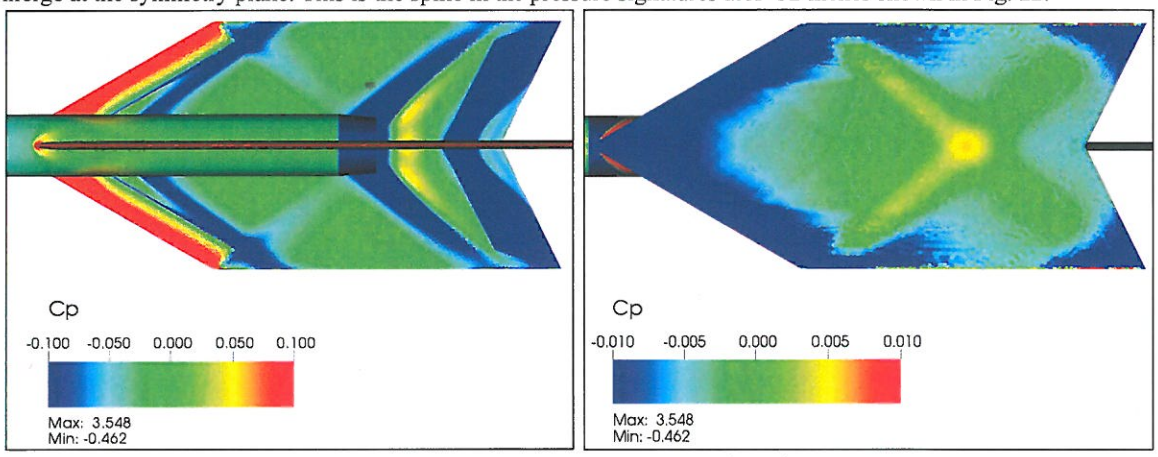


**a) Upper surface view** **b) Lower surface view**

**Figure 24. Pressure coefficient contours of the 2-diameter aft deck with 15° tip bevel angle, $M$=1.6, $NPR$=8.**

## G. Aft Deck Size and Shape

After the 1- and 2-diameter length decks were evaluated, concerns about the strength and size requirements of the blade strut arose. The 2-diameter deck area was 61.8 $in^2$ and the 1-diameter deck was 57.3 $in^2$, whereas the swept struts used by Lockheed in the N+2 studies (Refs. 1-2) supported models with maximum planform areas of 33.17 $in^2$. The strut in the present design requires a large cavity for high pressure air (HPA) and a small cavity for internal nozzle flow instrumentation wires as shown in a slice through the final designed strut perpendicular to it trailing edge in Fig. 25. Thus, it was apparent that the decks as originally designed were likely too large for the strut concept. Preempting any structural analyses, and realizing that by changing the NPR, the nozzle shocks could be placed both before and after a deck of intermediate size (between the 1- and 2-diameter decks). This would allow a single model that could shield or not shield nozzle exit shocks. Thus, the decks with 1- and 2-nozzle body diameter from the trailing edge were abandoned in favor of a smaller model with 1.8 nozzle-diameters to the trailing edge. The new deck planform with smaller area (39.9 $in^2$) is shown compared with the 1- and 2-diameter aft decks in Fig. 26. The decks are overlaid such that the nozzle exits are aligned. Figure 27 shows isometric and side views of the aft deck with the nozzle exit placed 1.8 nozzle diameters from its trailing edge.

**Figure 25. Interior view of the blade strut.**

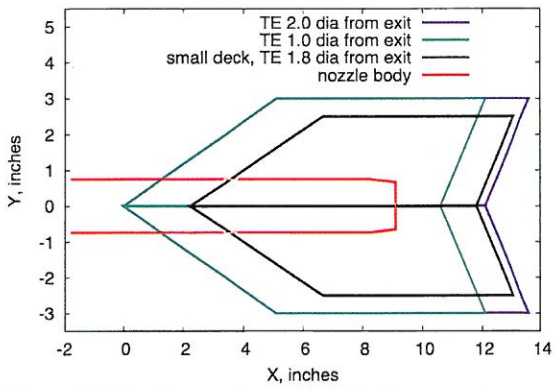


**Figure 26. Planform views of aft deck concepts.**

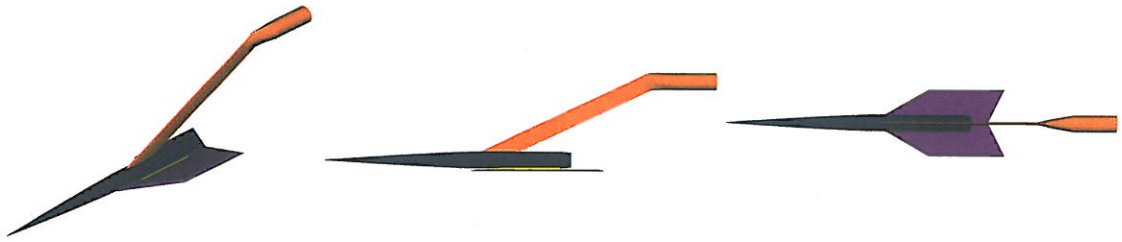

**a) Isometric view** **b) side** **c) top**

**Figure 27. Reduced size deck with nozzle exit 1.8 diameters from trailing edge.**

Density-gradient contours of the different sized decks are compared along with a solution without the deck component in Fig. 28. Different *NPR*s were not assessed due to the time constraints to quickly develop design

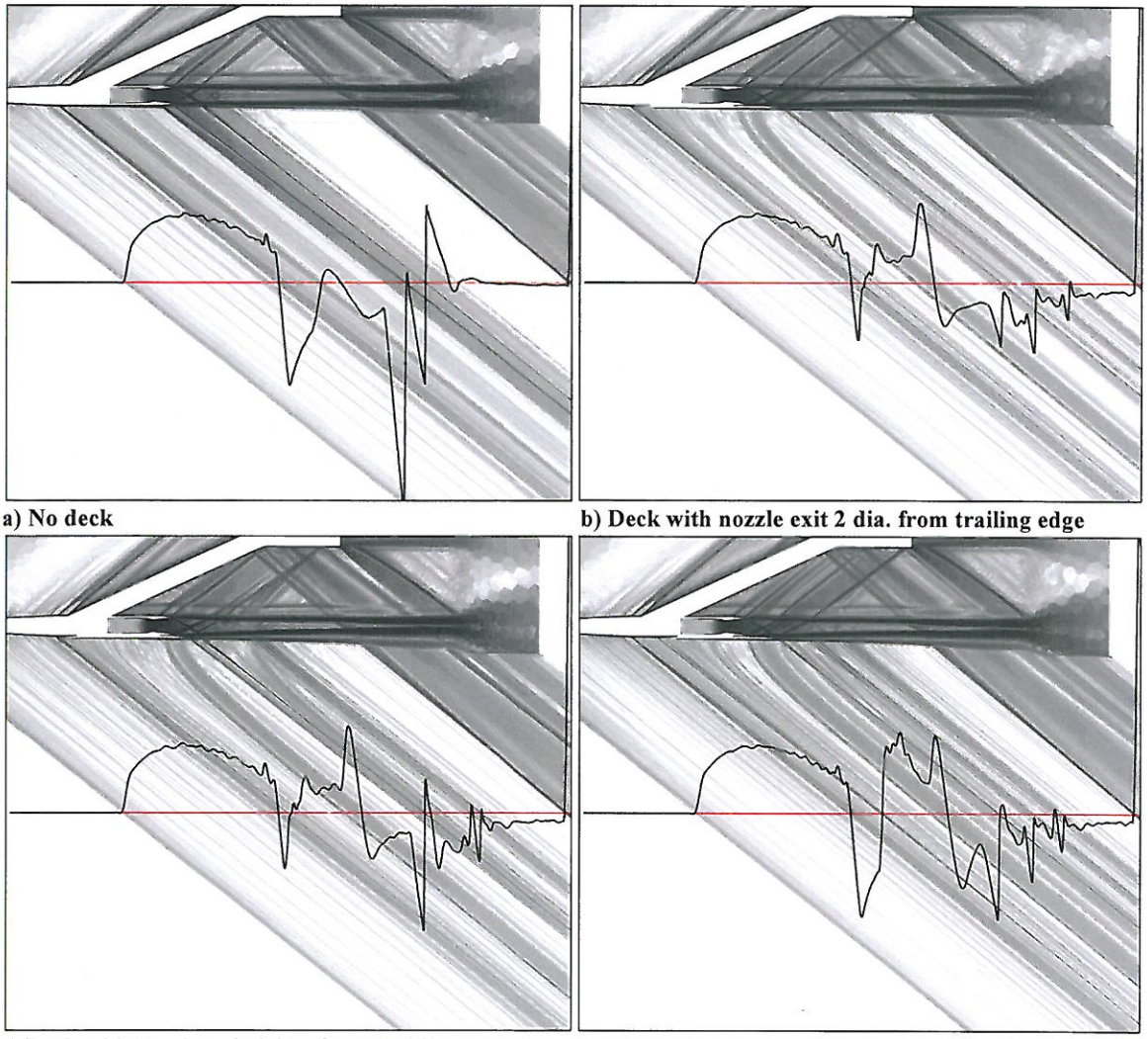

**a) No deck**

**b) Deck with nozzle exit 2 dia. from trailing edge**

**c) Deck with nozzle exit 1 dia. from trailing edge**

**d) Deck with nozzle exit 1.8 dia. from trailing edge**

**Figure 28. Density gradient comparisons of aft decks at 15 inches and *NPR* 8.**

configurations for testing. Later, the final deck will be evaluated for *NPR*s of 4, 8 and 14. The pressure signatures of the different aft-deck concepts are overlaid in Fig. 29. The large expansion shown without the deck provides a basis

for comparison of the shock shielding effects of the deck concepts. The 2-diameter aft deck possesses the most benign signature as expected. The 1-diameter aft deck has the same signature as the 2-diameter deck up to $X$=37 and then an expansion and shock follow from less shielding of the aft nozzle pressures. The 1.8-diameter deck has displaced shocks between $X$ of 27 and 35 inches from its reduced span and length, but the shocks from it appear no stronger than the 1-diameter deck at *NPR* of 8. The 1.8-diameter deck was sized such that the nozzle shock was just behind the trailing edge of the deck, and it was anticipated that with reduced *NPR* more shielding would occur and with increased *NPR* less shielding would occur. Without time for computational validation of this, the 1.8-diameter aft deck concept was selected as the 2nd design for testing.

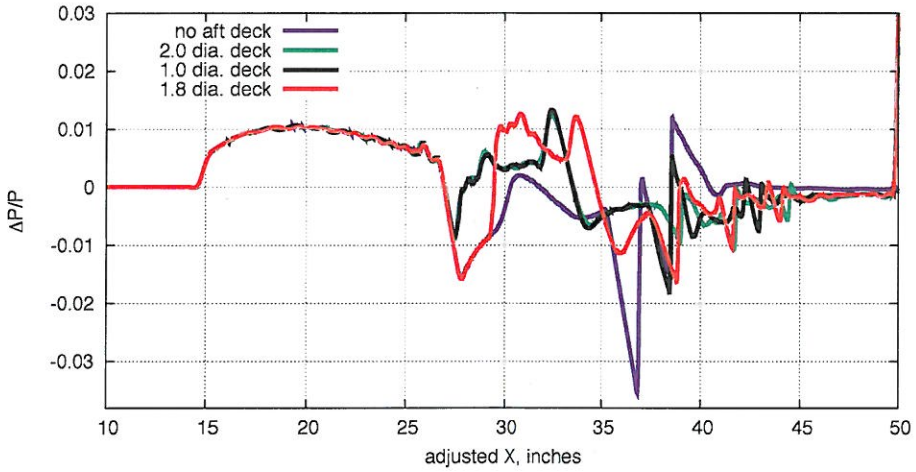


**Figure 29. Comparison of aft deck pressure signatures at 15 inches and *NPR* 8.**

## H. LaRC-25D Tail Shock Generator

The 3rd configuration selected for testing is referred to as the LaRC-25D tail. It is the same size (6.65 inch root chord) relative to the nozzle diameter as the vehicle concept designed for low sonic boom (Ref. 30) at Langley Research Center (LaRC). The tail of the vehicle concept has a detailed camber design and is well integrated into the configuration design for very low sonic boom characteristics. The tail here employs a biconvex section and it is placed in the same location relative to the nozzle exit as the vehicle configuration. The reasons for inclusion of the LaRC-25D tail are:

- Represents a tail from a modern (non-proprietary) low boom vehicle
- Tail size relative to nozzle size is realistic
- Three-dimensional effects greater due to the size

The LaRC-25D SG required a 2-inch nozzle extension in order to position the tail further aft on the strut while retaining the tails position relative to the nozzle exit. Without the nozzle extension the leading edge of the 25D SG was aft of the strut leading edge. With the nozzle extension the LaRC-25D tail shields the shocks from the upper portion of the strut. Figure 30 shows isometric, side and top view of the test configuration.

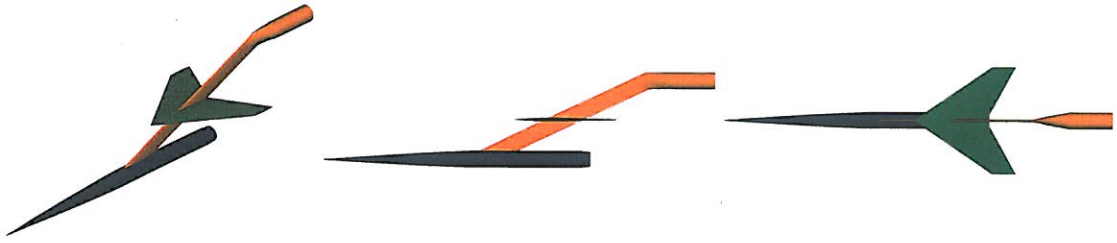

**a) Isometric** **b) Side** **c) Top**

**Figure 30. Three views of the LaRC-25D shock generator.**

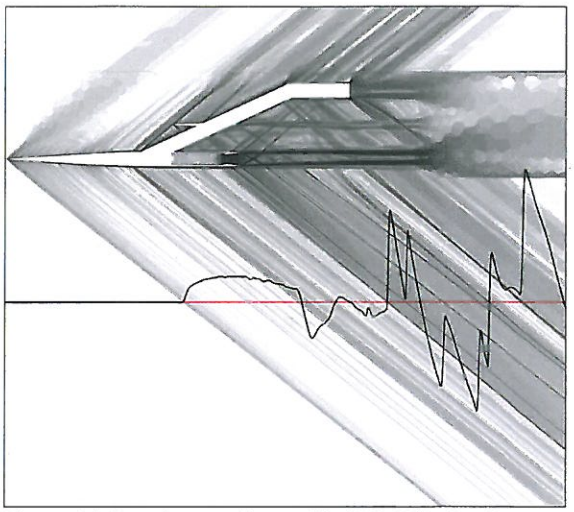

**Figure 31. Density gradient of LaRC-25D shock generator at 15 inches and *NPR* 8.**

The outline of the tail and strut can be seen in Fig. 31 of the symmetry plane with density gradient contours at Mach 1.6. The pressure signature has multiple shocks that are greater in strength than the biconvex SG at 0° angle of attack (Fig. 32). The LaRC-25D has slightly greater signal strength than the biconvex at 4° (compare with Fig. 20), and this larger model will produce greater on- and off-track signature with increased angle of attack than the biconvex SG. The strut is too short in this initial concept; the shock from the sting portion is contaminating the signature before ambient flow has been achieved. In Fig. 32, the strut-sting shock at $X$=51 inches appears before the SG trailing shock at $X$=47 inches has returned to a pressure of zero. In the final design, the strut was lengthened based on this finding.

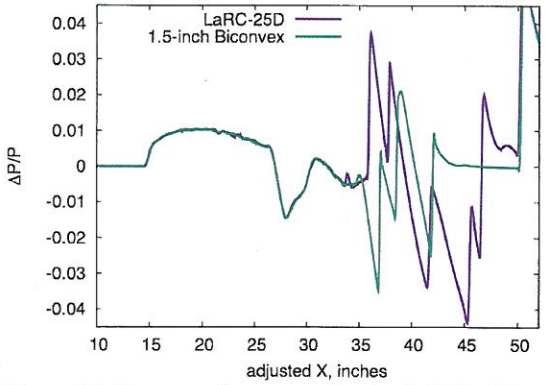


**Figure 32. Pressure signatures for the LaRC-25D overlaid with the biconvex at 15 inches and *NPR* 8.**

## I. Double Wedge Shock Generator

The fourth and final design provided at the PDR was a 2.25 inch chord double-wedge shock generator with 5° half angle leading and trailing edges. It was selected for testing because it was previously tested in the 1x1-Foot Supersonic Wind Tunnel at GRC with a 1-inch outer nozzle diameter. Here, the model was scaled up so that its size and position to the nozzle exit center were proportional to the nozzle body diameter. The existing nozzle body length would not allow for the SG to be placed at the required vertical distance from the nozzle exit center with the 1.5-inch outer diameter body. In order to accomplish this, a 4-inch nozzle extension will be manufactured. Figure 33 shows the double-wedge shock generator with the extended nozzle configuration in isometric, side and top views.

**a) Isometric front view** **b) Side view** **c) Top view**

**Figure 33. Three-view of the double-wedge shock generator.**

The shocks from the non-swept, non-tapered, and approximately 9-percent thick shock generator are significantly larger than the former swept biconvex SG configuration with a 5-percent thick root section (Fig. 34 and 35). This conceptual design, like the LaRC-25D, also has insufficient strut length for the flow to return to ambient conditions, and the trailing shock of the double wedge has coalesced with the sting-strut shock. Although, the analysis of the double wedge was performed at Mach 1.6, the experiment is planned for Mach 2.0 to tie in with the former 1x1-foot test data of this SG. On the final design, a Mach 2.0 computation is presented.

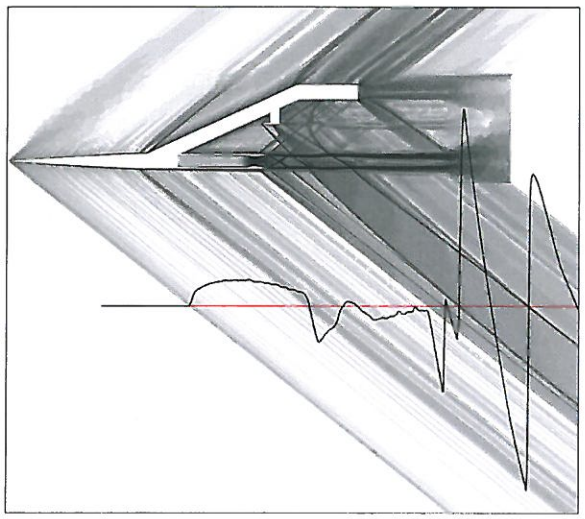

**Figure 34. Density gradient of the double-wedge shock generator at 15 inches and *NPR* 8.**

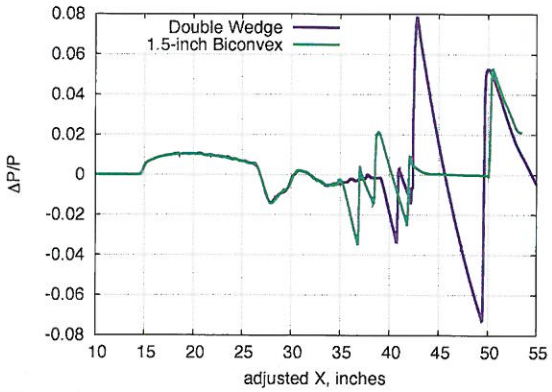


**Figure 35. Pressure signature for the double-wedge shock generator at 15 inches and *NPR* 8.**

Four configurations from these studies were selected for inclusion in the experiment: the 1.5 inch biconvex, the small aft-deck with nozzle exit 1.8 dia. from trailing edge, the 6.65 inch LaRC-25D, and the 2.25 inch double wedge. At the time of the preliminary design review, dense surface meshes of these configurations in STL (Stereo Lithography) format were read into CAD software, drawings were made, and then analytic surfaces were generated, except for the forebody, where the equation was provided. The analytic shapes developed with CFD code analyses were the starting definition for the wind tunnel models. As expected, it was necessary to make many but mostly limited modifications for implementing cost effective mounting hardware and other instrumentation designs changes. CAD surfaces, both external and internal to the actual hardware that would satisfy structural load requirements in the supersonic flow of the 9x7-Foot Wind Tunnel were developed. These CAD-based representations are referred to as the PDR models or configurations.

## V. PDR Model Analyses

The solutions of the PDR configurations are presented at Mach 1.6 and a *NPR* of 8.0. The CAD surfaces were used as the defining outer mold lines of the configurations and high quality surface meshes were developed using *ANSA*. The surface meshes were then transferred into *STAR-CCM+* where volume meshes suitable for accurate sonic boom computations with the Navier-Stokes equations were developed. The resulting meshes used for these computations were of higher quality than the meshes used for design.

### A. Biconvex (PDR)

A few representative images of the surface mesh are shown for the biconvex SG configuration in Fig. 36. Meshes will not be shown for the other configurations because they are of the same quality. The surface mesh shown is of the polyhedral mesh generated in *STAR-CCM+* from a mixed element surface mesh composed of triangles and quadrilaterals generated in *ANSA*.

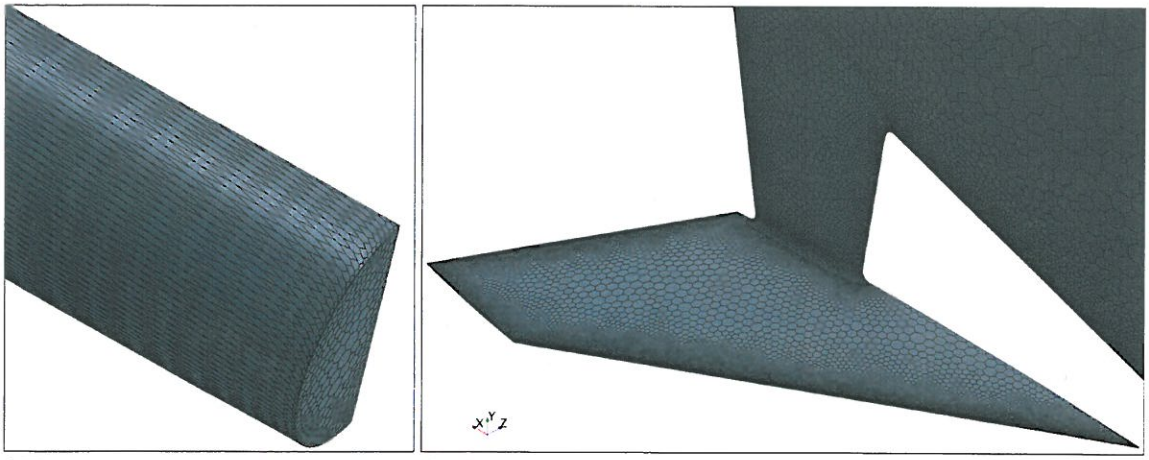

**a) Nose** **b) Biconvex shock generator, down strut, and main strut**

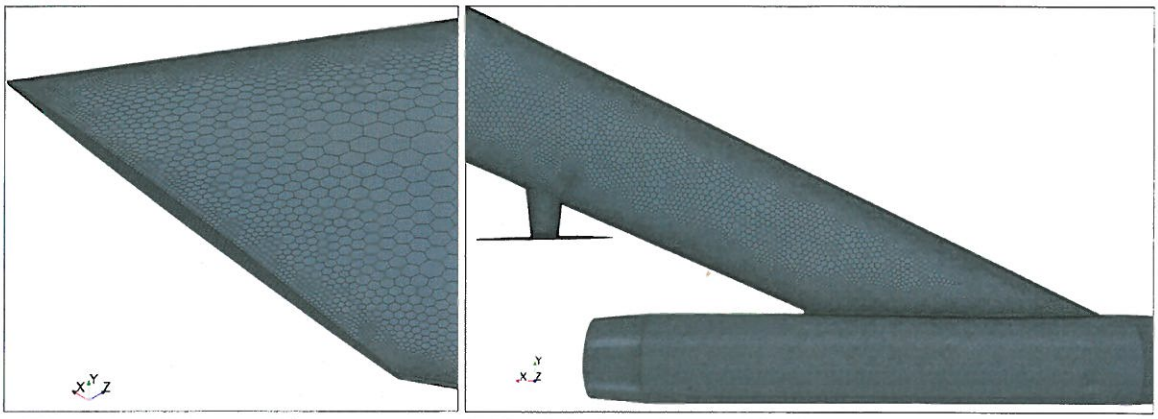

**c) Tip region of biconvex SG** **d) Nozzle-body and strut (side view)**

**Figure 36. Polyhedral surface mesh typically used for accurate sonic boom computations with *LAVA*.**

The refined volume mesh within the near-body cylinder was generated with *STAR-CCM+*. The symmetry plane mesh is shown in Fig. 37. As previously mentioned the Mach aligned cells were generated with an in-house program that generates hexahedral cells from the cylindrical region to several body-lengths away. The configuration is placed within a small cylinder so that the Mach aligned cells begin close to the body for efficient use of mesh points, reduced dissipation in the solution, and more accurate pressure signatures. A refinement region in the plume region was developed for improved solution accuracy of the shock interactions with the nozzle jet plume. Solutions with the quadrilateral cells appended to the volume mesh were then obtained with the unstructured-grid flow solver within the *LAVA* framework. The computations were preformed on the NASA Advanced Supercomputing (NAS) computer, Pleiades. Solutions typically used 720 processors and were obtained in less than 4 hours. The number of cells varied between 26.5- and 49.2-million, the LaRC-25D required the largest mesh.

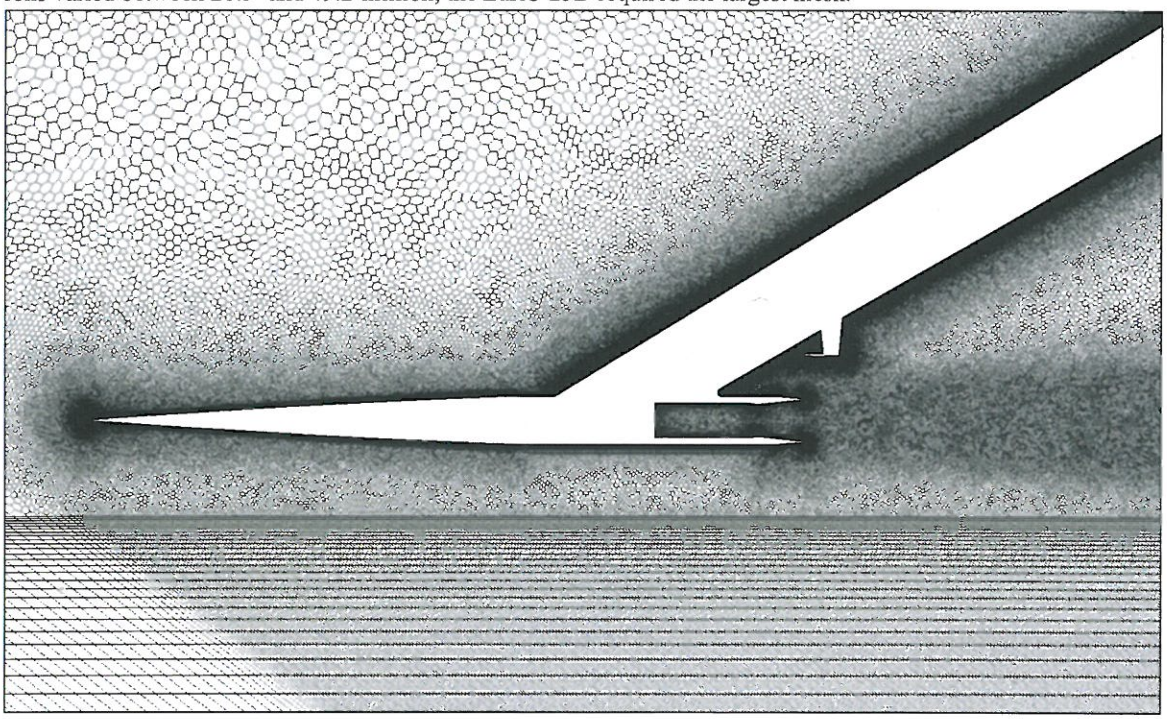

**Figure 37. Symmetry plane mesh of polyhedra.**

The solution of the four designs from the PDR, with properly sized strut and model supporting hardware and HPA lines at the top of the blade strut are shown in Fig. 38. A significant portion of the test hardware aft of the blade strut is modeled in the computations to allow for the assessment of the shock(s) strength and position from the

support system. These solutions affirm that the model supporting hardware and HPA lines' shocks do not interfere with the trailing shocks of any of the shock-generation models, including the LaRC-25D and double wedge shock generators. There is ample distance between the trailing shocks from all SGs before the supporting hardware and HPA line shocks are encountered to achieve pressure levels of ambient flow. This indicates that the strut is now long enough, eradicating the previously noted design flaw. Note that the shocks from the model supporting hardware are of greater strength and the angle of the shocks is smaller than most model shocks. Thus, at some greater distance the shocks from the support hardware will approach the models shocks and coalesce, but not within the 35-inch testing range planned for the upcoming test.

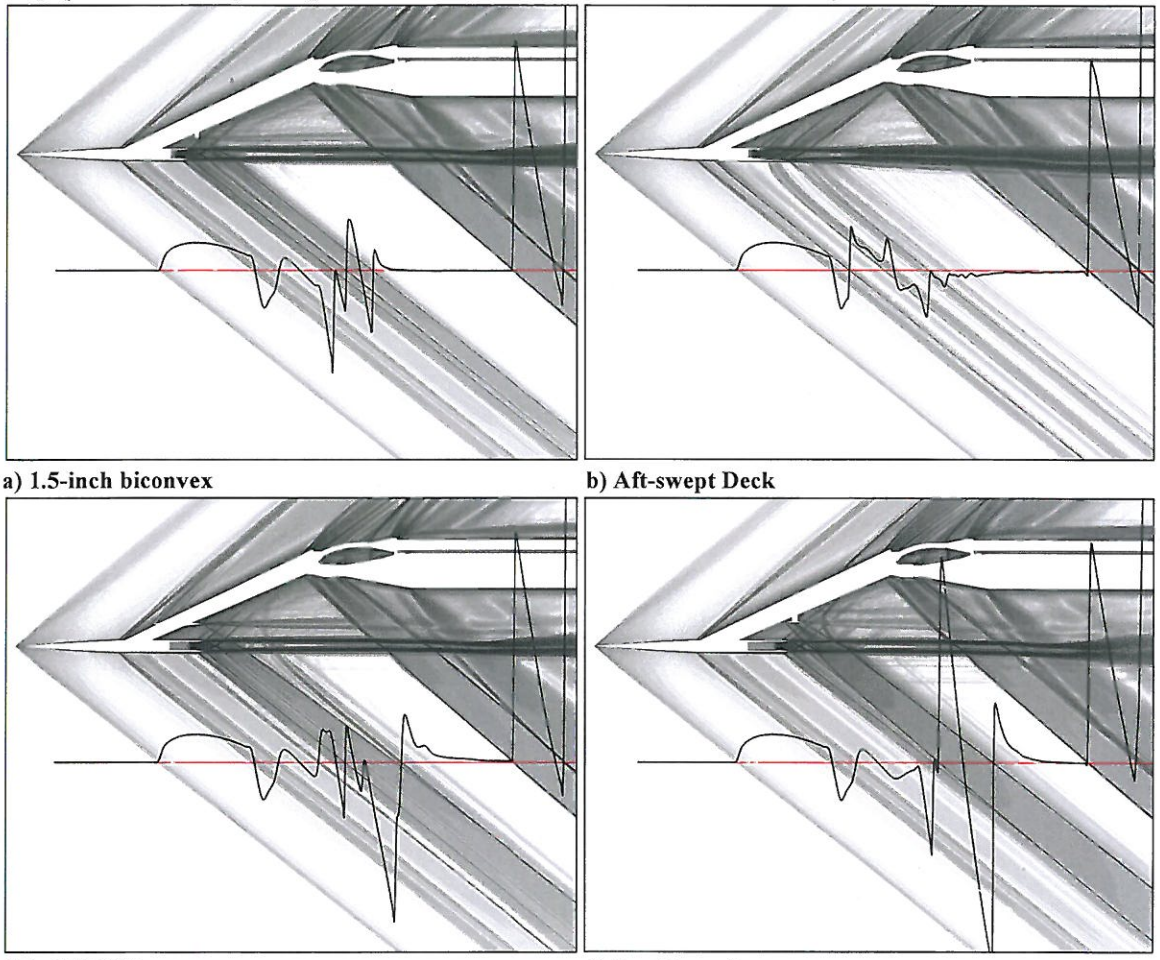

**a) 1.5-inch biconvex** **b) Aft-swept Deck**

**c) LaRC-25D** **d) Double-wedge**

**Figure 38. Density contours and overlaid pressure signatures for the PDR OMLs from CAD.**

The pressure signatures are shown for altitudes of 7, 15, 25, and 35 inches for the four models in Fig. 39. The signatures are shifted such that the leading shocks are aligned and truncated after the first downstream shock from model supporting hardware is encountered. Note that different Y-axis scales are shown in the figure to provide pressure signature details in the space available within each plot. Here, the forward movement of the model-support hardware shocks is evident and these shocks have moved forward about 4 inches from altitudes of 7 to 35 inches.

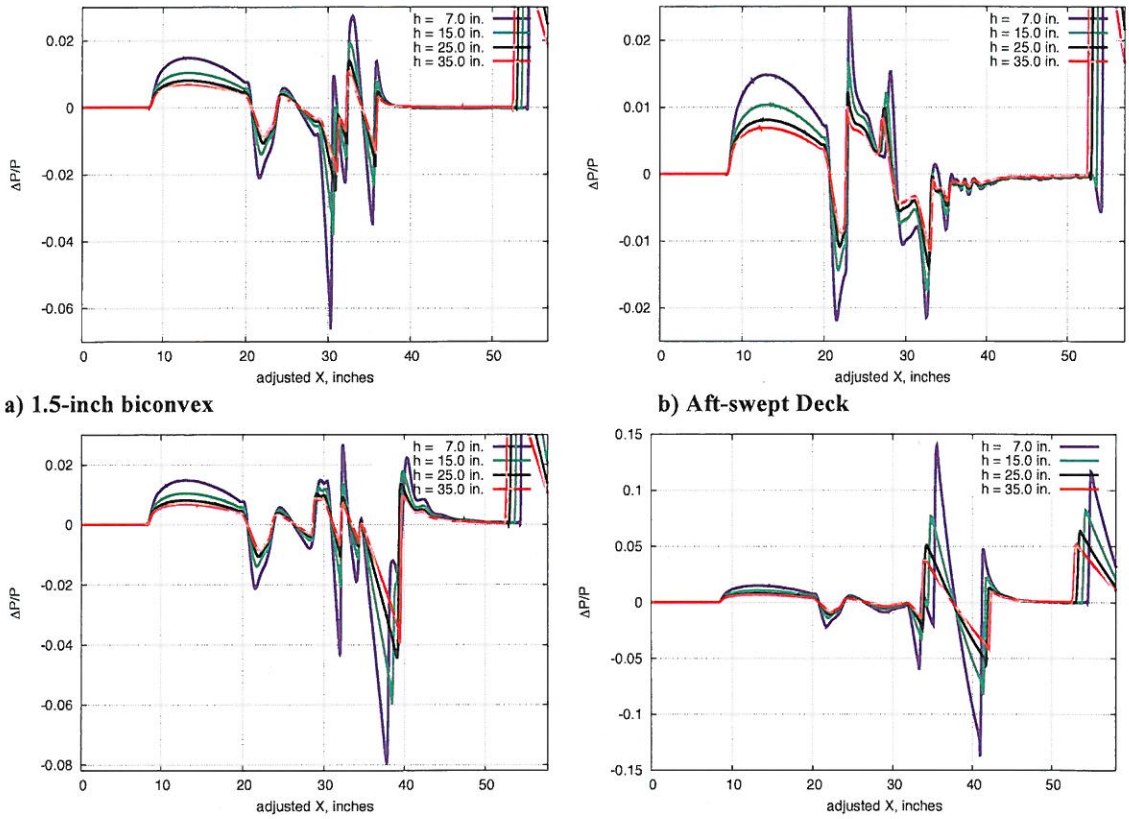


a) 1.5-inch biconvex

b) Aft-swept Deck

c) LaRC-25D

d) Double-wedge

**Figure 39. Pressure signatures for the PDR OMLs from CAD.**

## VI. Revision of Model

NASA's industry partners cautioned that the initial CAD design may have some regions of separated flow on the blade strut, based on experimental oil flow patterns on their N+2 strut designs with similar sweep and thicknesses. The separated flow on the aft part of the strut is due to the large sweep (particularly the sweep of the trailing edge if the strut is tapered) and the thickness. A photograph of the oil flow patterns after exposure to the supersonic flow in the 9x7 is shown for a 70° plate attached to LM phase II swept strut in Fig. 40. The photo shows that boundary layer trip disks of 0.05-inch diameter and 0.0075-inch height were affixed to the blade strut. A red arrow points to one of the disks in the figure. The blade struts' sweep is 72.9° relative to free-stream and its streamwise thickness/chord ratio at the tip (near the plate) is 10.1%, and at its root 13.6%. The disks were not intended to fully trip the boundary layer, but rather to energize it to delay separation. There is no evidence of spanwise spreading of the turbulent regions downstream of the disks in the photograph so the boundary is not tripped. The disks may have reduced the amount of separation on the aft strut, but without an oil flow without disks, it is not known if they were effective. The test team would like to test with and without disks to determine if they are beneficial or not, but with the limited test time in the tunnel, it may not be possible.

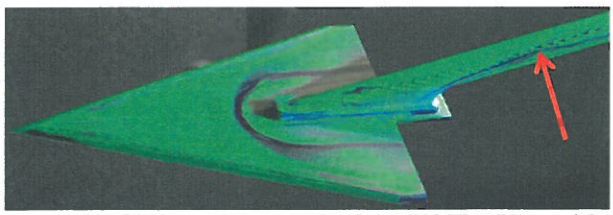

**Figure 40. Oil flow photograph of the 70° Flat Plate with the 72.9° swept strut from N+2 test.**

It was decided that some precautionary changes should be made to the PDR design to help minimize separation on the strut. The trailing edge sweep, with the struts taper, was 67.5°. Because of the former computational analyses with 60° and 65° sweep angles (Fig. 6 and 7), changing to a 60° sweep strut was known to have acceptable shock

strength. Therefore the trailing edge sweep angle was modified to 60° and taper was applied only to the leading edge. Changing the strut sweep required all of the shock generators positions to change, and the development of new attaching struts. In addition, the strut was lengthened to ensure at least as much shock free distance from the trailing edge of each SG to the shock from the attachment hardware in the nozzle plume region, as well as many other changes. The three SGs retained their position relative to the nozzle exit center and the deck retained its size, but the blade strut was moved back on the nozzle (0.45 in. from cylinder to strut leading edge on PDR and 1.247 in from cylinder to strut leading edge on final design). This was done to ensure equivalent or greater shielding with the deck with the expected stronger strut shock from the 60° swept strut. The thickness/chord ratios normal to the leading edge were 14.3%, but streamwise ratios of 7.6 and 6.7 percent result for the 60° and 65° struts, respectively.

*LAVA* solutions are shown in Fig. 41 for the PDR and final designs in laminar and turbulent flow fields. It is expected that the laminar solutions over-predict separation, and that the experimental data may yield results between the laminar and fully turbulent flow predictions. Surface pressure coefficient (Cp) is shown along with plotted data at a single position on the strut, with its location indicated by the red lines in the plots. In the top half of the figure results with the former PDR strut are shown, and in the bottom half are the new final design results. A very uniform pressure distribution is seen in the final design with the Spalart Almaras (SA) turbulence model. Whereas, the turbulent flow solution of the PDR design has a small hump at 80-percent chord in the pressure distribution. This is an indication that the final design is less likely to separate than the PDR design. Also, the turbulent and laminar solutions of the final strut have more uniform color contours across the entire strut surface than the PDR design. The amount of separation on the final design is expected to be minimal from these results. But, these results are not conclusive because flow in the wind tunnel is not fully turbulent. However, it is clear that there has been a beneficial change in the Cp distribution over the strut surface in the revised 60° strut. The laminar result of the 65° strut appears like the flow is separated at 90 percent chord, and the laminar pressure distribution of the 60° strut has a steep adverse pressure gradient that is likely unstable.

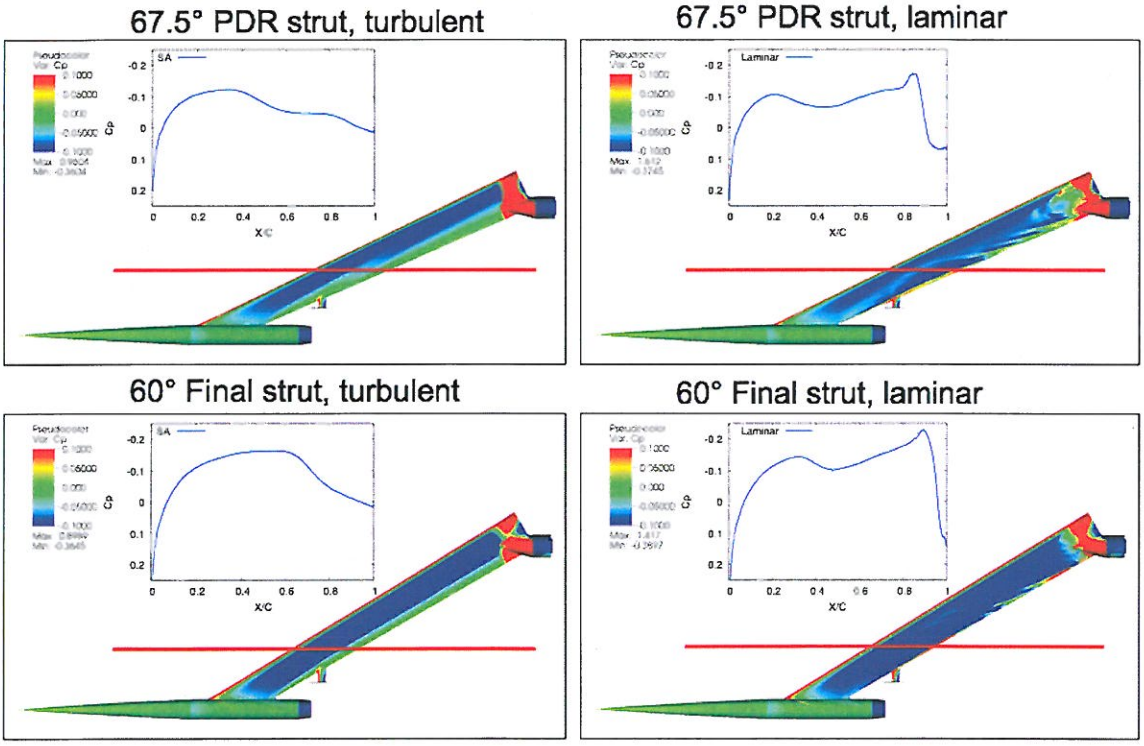


**Figure 41. Pressure coefficient comparison of laminar and turbulent flow solutions for PDR and final designs.**

## VII. Final Model Designs Analyses

Similar gridding techniques were employed on the final design as were used on the PDR models. Density gradients on the symmetry plane are shown for the final five design configurations computed at a Reynolds number of $4.5 \times 10^6$ per foot in Fig. 42. The fifth design was included in the mix without preliminary CFD results. It is a

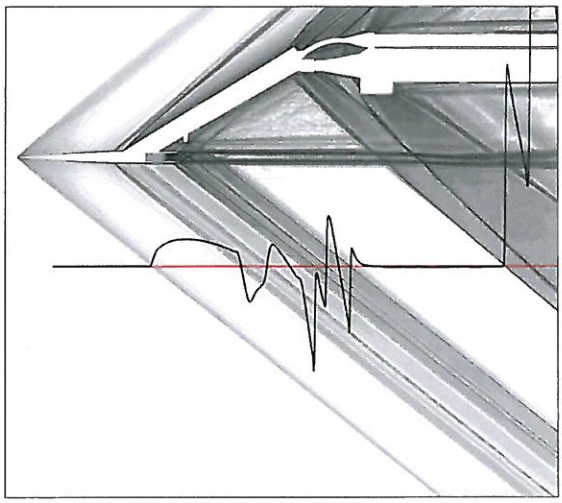

a) 1.5-inch biconvex

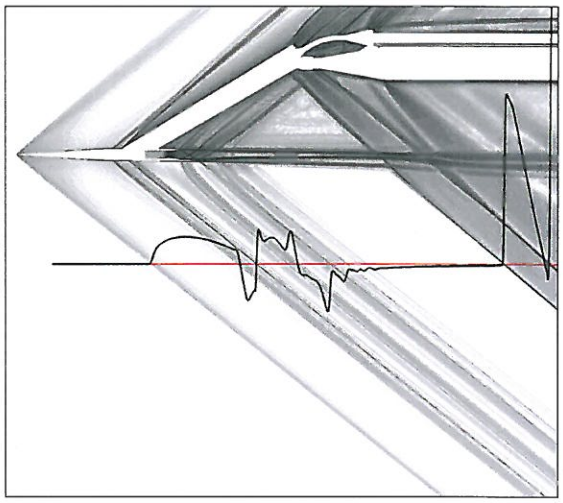

b) Aft-swept deck

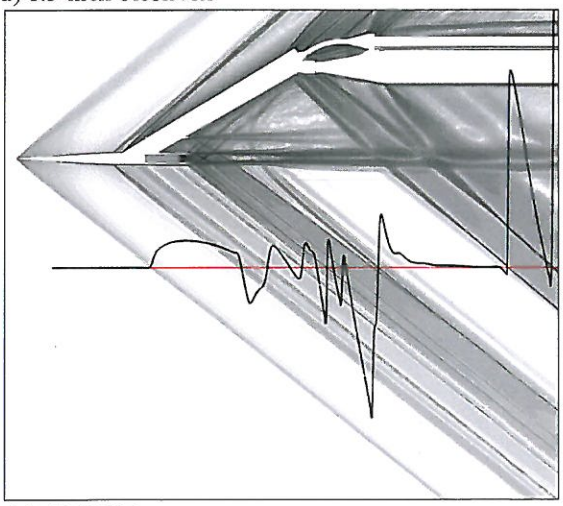

c) LaRC-25D

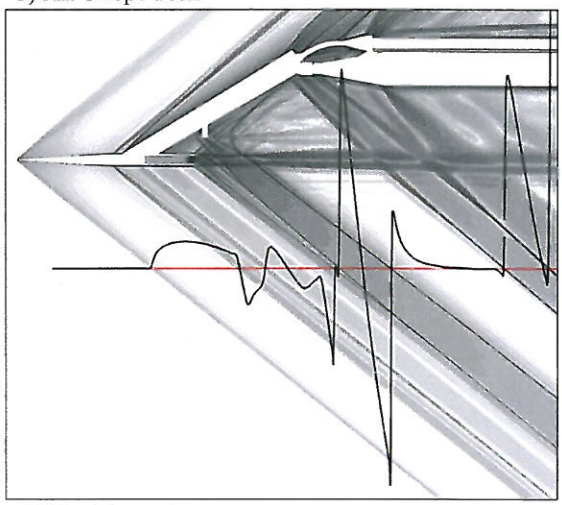

d) Double-wedge

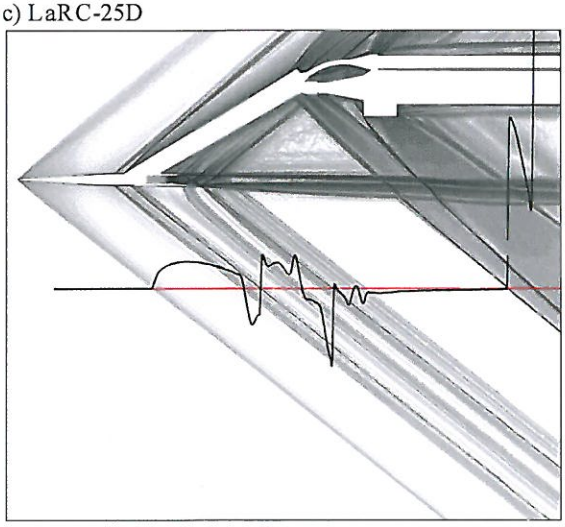

e) Forward-swept deck

Figure 42. Density contours and overlaid pressure signatures for the final design OMLs from CAD.

forward swept aft-deck configuration, with identical leading edge sweep and span to the aft-swept deck. The deck sweeps forward at the opposite sweep angle of the aft-swept deck. The final pre-test CFD pressure signatures are shown for each model at altitudes of 7, 15, 25, and 35 inches in Fig. 43. A companion paper also evaluates these final designs with a different grids and flow solver (Ref. 32). The pressure signatures in Fig. 43 are plotted to the same scale as the PDR design results shown in Fig. 39 for easy comparison. The final design with the 60° swept strut offers a larger range of shock free data in the plume region. For example the supporting hardware and HPA line shocks are encountered at about 57 inches in the final design whereas in the PDR design, shocks appear around 54 inches. The strut was lengthened to account for the reduced sweep, so that the axial distance between the nozzle exit and attaching hardware was equal, which results in a larger shock free plume region because of the added travel for the shock waves. This allows the trailing shocks from the shock generators to return to ambient condition.

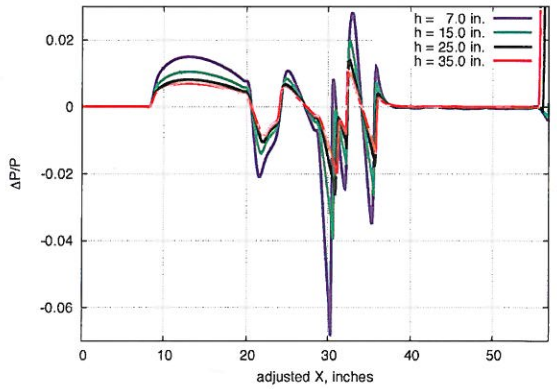


**a) 1.5-inch biconvex**

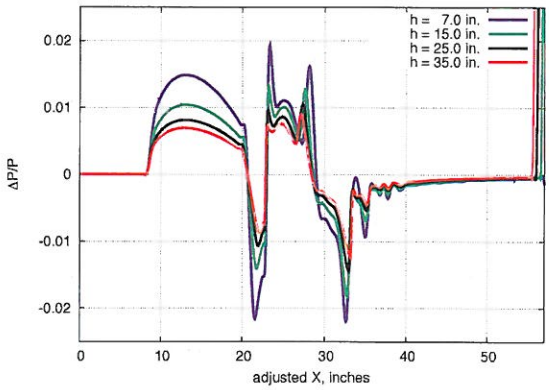


**b) Aft-swept deck**

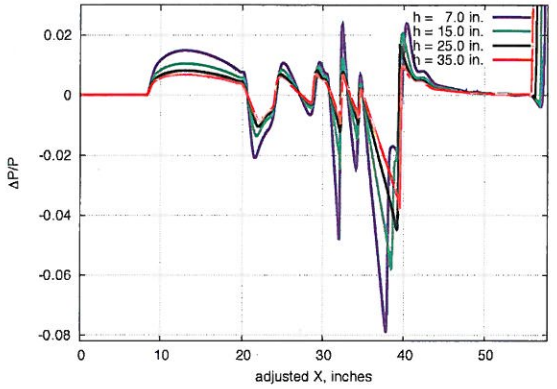


**c) LaRC-25D**

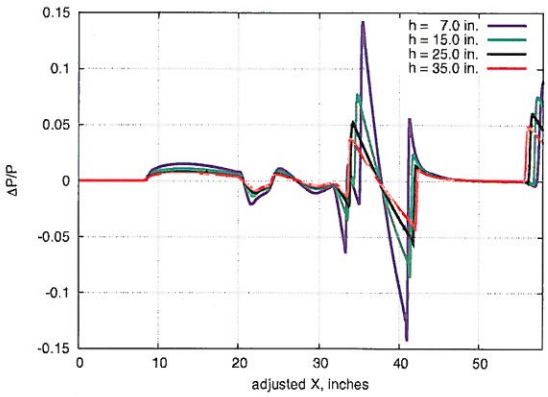


**d) Double-wedge**

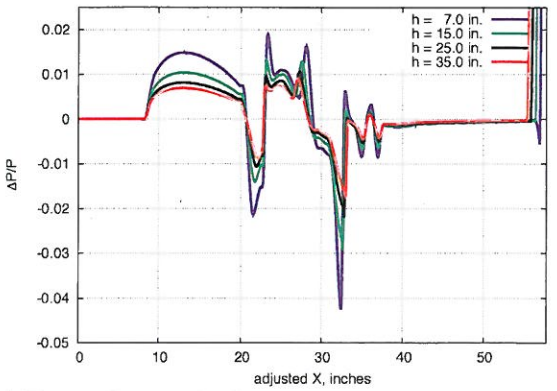


**e) Forward-swept deck**

**Figure 43. Pressure signatures of final design configurations *M*=1.6, *NPR*=8.**

The forward swept deck signatures in Fig. 43e should be compared with the aft-swept deck signatures in Fig. 43b. As expected the forward swept deck offers significantly less shielding, and note the expanded pressure coefficient range required for the forward swept deck in Fig. 43e.

The aft deck configuration was run with *NPR* of 4 and 14, representing the lower and upper bounds of the *NPRs* that will be assessed in the wind tunnel test, in order to verify that different levels of shielding can be obtained with the single aft deck design. The *NPR* 4 result has good shielding without the large expansion and shock that are seen at *NPR* of 14 (Fig. 44). The pressure signatures at 4, 8, and 14 are overlaid in Fig. 45, where there is little difference in the *NPR* 4 and 8 results.

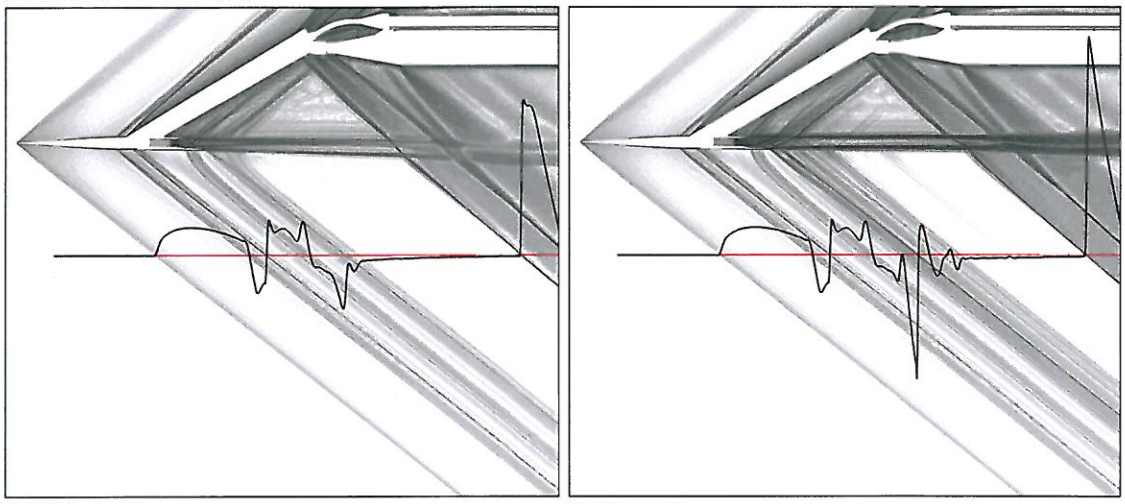

**a) *NPR*=4** **b) *NPR*=14**

**Figure 44. Density contours at bounding *NPR* values with the aft-swept deck, *M*=1.6.**

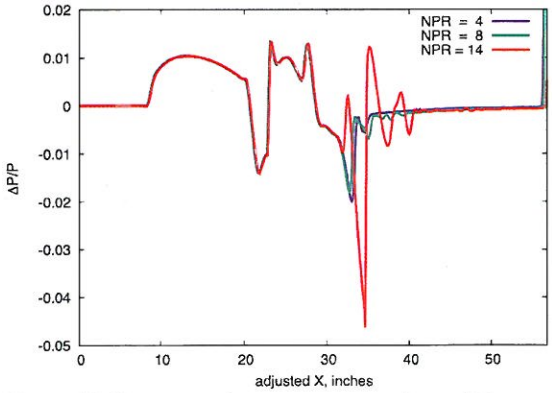


**Figure 45. Pressure signature comparison of three *NPRs* with the aft-swept deck, *M*=1.6.**

The double wedge shock generator is a scaled model of the shock generator tested in the GRC 1-by-1-Foot tunnel at Mach 1.96. The priority is to run the double wedge at the same Mach number as previously tested at GRC. The data in the plume region will also be reflection free at this Mach number, whereas at Mach 1.6 the bow shock from the model nose reflects before the shock from the model support hardware is encountered. Fig. 46 shows a layout diagram at Mach 2.0 for the double wedge SG. This model extends a little further aft and higher on the strut than the other models so its trailing shock will be further aft and closer to the strong shock from the model assembly. At Mach 2, the layout diagram shows that the model nose shock (light blue) reflects off the tunnel wall and strikes the rail only a couple of inches before the model support shock (red) strikes the rail (around tunnel station of -85 inches). The layout shown in Fig. 2, reveals that the reflected nose shock strikes the rail about 12 inches upstream of the model support shock, but has 12 inches behind the deck trailing shock before the reflected nose shocks strikes. If there is need for downstream plume evaluation, increasing the Mach number increases the aft plume region of shock-free flow. It should be easy to tell if the reflected nose shock is affecting the signatures since the predicted signature is flat after it has returned to ambient condition and of value 0.0. If not, the deviation in pressure is from the model nose reflecting from the tunnel wall at the base of the pressure rail.

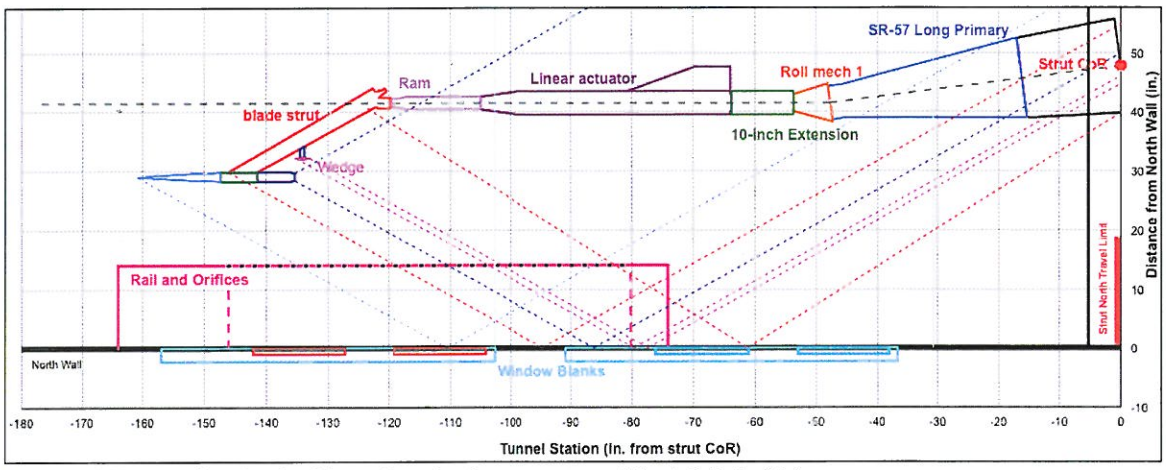


**Figure 46. Layout for the double wedge shock generator at Mach 2.0, *h*=15 in.**

Figure 47 shows the density gradients on the symmetry plane at Mach 2.0, and the pressure signatures at 15 inches are overlaid with the Mach 1.6 results in Fig. 48. The Reynolds number used in the computations was $3.8 \times 10^6$ per foot.

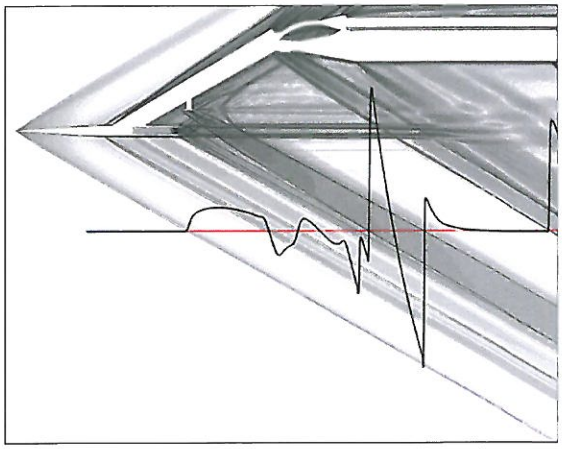

**Figure 47. Density contours of the double wedge at Mach 2.0**

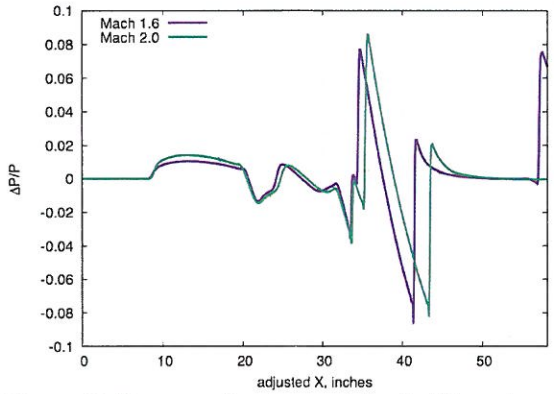


**Figure 48. Pressure signatures of the double wedge at Mach 2.0 compared with Mach 1.6, *h*=15 *in.*, *NPR*=8.**

## VIII. Concluding Remarks

In support of an upcoming test in the Ames 9- by 7-Foot Supersonic Wind Tunnel, CFD was used to manually design a series of test configurations to assess the effects of pressure waves passing through nozzle jet flow on the sonic boom pressure signatures. Many aspects of the test-configuration design were studied with CFD: forebody shape, strut sweep angle, nozzle-body size, full configuration pitch rotation versus shock generator rotation, the effect of nozzle pressure ratio, aft deck size, shape, and deck bevel angles, and small and large swept and un-swept shock generators. Navier-Stokes computations of more than 45 test-model concepts provided the knowledge of the surrounding flowfield with complex pressure/nozzle jet flow interactions to make intelligent design decisions to arrive with a reduced set of five test models that provide a variety of shapes representative of aft aircraft components. The final five test models include a 1.5 inch nozzle-body with an analytic forebody that provides similar overpressure levels of a modern low boom concept and one of the following shock generators: a small 1.5 inch root chord biconvex, a large 6.65 inch chord biconvex with the planform of the LaRC-25D low boom demonstrator, an un-swept 2.25 inch chord double-wedge, and 9.55-inch aft-swept and forward-swept deck concepts.

Data from the planned experiment will allow industry and government to apply their current best-practice computational meshing and flow solver algorithms to the test articles and compare sonic boom pressure signature results. These comparisons will promote advancement of grid generation techniques and/or flow solver for greater confidence in their sonic boom predictive capabilities of the aft portion of the sonic boom pressure signature.

The planned experiment is a good next step towards the study of nozzle plume and shock interactions, but it is not clear if cold jet nozzle flow at low Reynolds number with this variety of configurations is sufficient to meet the needs of industry, or if the highly integrated components in the aft portion of a modern low boom aircraft can only be evaluated by flight testing a specific model.

## IX. Acknowledgments

The authors appreciate the support of the NASA Fundamental Aeronautics Program Commercial Supersonic Technologies Project, and are grateful to Emre Sozer, formerly with Sciences and Technology Corporation (STC) at Ames Research Center, for his contributions towards accurate sonic boom predictions with the unstructured-grid solver within the *LAVA* framework, and James Jenson (with STC at Ames) for geometry and computational analyses. We thank Raymond Castner from Glenn Research Center for sharing his experiences and advancing nozzle plume with shock interactions wind tunnel testing, and our CFD/test team for their contributions: Alaa Elmiligui, Melissa Carter, Courtney Winski, Jason Pearl, and Linda Bangert from Langley Research Center. We also thank our industry partners for their expertise and guidence; John Morgenstern and Mike Buonanno form Lockheed-Martin Aeronautics; Eric Adamson, Todd Magee, and Steve Shaw from The Boeing Company; and Robbie Cowart, Tom Wayman, and Kenrick Waithe from Gulfstream.

## X. References

[1]Morgenstern, J., Norstrud, N., Sokhey J., Martens, S., and Alonso, J., "Advanced Concept Studies for Supersonic Commercial Transports Entering Service in the 2018 to 2020 Period", Phase I Final Report, NASA/CR—2013-217820, February 2013.

[2]Morgenstern, J., "Final Report for the NASA N+2 Supersonic Validations Phase II: Advanced Concepts Studies for Supersonic Commercial Transports Entering Service in the 2018 to 2020 Period", NASA/CR—2013-X, 2013. Report not yet published.

[3]Magee, Todd E., Wilcox, Peter A., Fugal, Spencer R., Acheson, Kurt E., Adamson, Eric E., Bidwell, Alicia L., and Shaw, Stephen G., "System-Level Experimental Validations for Supersonic Commercial Transport Aircraft Entering Service in the 2018–2020 Time Period, Phase I Final Report," *NASA CR-2013-217797*, February 2013.

[4]Magee, Todd E., Shaw, Stephen G., and Fugal, Spencer R., "Experimental Validations of a Low-Boom Aircraft Design," *AIAA Paper-2013-0646*, 51st AIAA Aerospace Sciences Meeting, Dallas TX, January 2013.

[5]Magee, Todd E., Fugal, Spencer R., Fink, Lawrence E., Adamson, Eric E., and Shaw, Stephen G., "System-Level Experimental Validations for Supersonic Commercial Transport Aircraft Entering Service in the 2018–2020 Time Period, Phase II Final Report," *NASA CR (to be published).*

[6]Magee, Todd E., Fink, Lawrence E., Fugal, Spencer R., Adamson, Eric E., and Shaw, Stephen G., "Boeing N+2 Supersonic Experimental Validation Phase II Program," *AIAA 2014–2137*, 32nd AIAA Applied Aerodynamics Conference, Atlanta GA, June 2014.

[7]Putnam, L., and Capone, F., "Experimental Determination of Equivalent Solid Bodies to Represent Jets Exhausting into a Mach 2.20 External Stream," *NASA TN-D-5553*, 1969.

[8]Castner, Raymond, Elmiligui, Alaa, Cliff, Susan, and Winski, Courtney, "Plume and Shock Interaction Effects on Sonic Boom in the 1-foot by 1-foot Supersonic Wind Tunnel," *AIAA 2015-1046*, 53rd AIAA Aerospace Sciences Meeting, Kissimmee FL, January 2015.

[9]Castner, Raymond, "Exhaust Nozzle Plume Effects on Sonic Boom," *Journal of Aircraft*, Vol. 49, No. 2, March-April 2012.

[10]Castner, Raymond S., "Cart3D Analysis of Plume and Shock Interaction Effects on Sonic Boom," *AIAA 2015-2263*, 33rd AIAA Applied Aerodynamics Conference, Dallas TX, June 2015.

[11]Housman, Jeffrey A. and Kiris, Cetin C., "Numerical Simulations of Shock/Plume Interaction Using Structured Overset Grids," *AIAA 2015-2262*, 33rd AIAA Applied Aerodynamics Conference, Dallas TX, June 2015.

[12]Carter, Melissa B., Nayani, Sudheer, Elmiligui, Alaa A., and Campbell, Richard L., "USM3D predictions of Supersonic Nozzle Flow," *AIAA 2014-2270*, 32nd AIAA Applied Aerodynamics Conference, Atlanta, GA, June 2014.

[13]"Test Planning Guide for High Speed Wind Tunnels"
*http://www.nasa.gov/sites/default/files/643643main_HSpeedTestPlanGuide.pdf.*
NASA Ames Wind Tunnel Operations Division report number A027-9391-XB2, rev. 5, April 27, 2005

[14]Reed, T. D., Pope, T. C., and Cooksey, J. M., "Calibration of Transonic and Supersonic Wind Tunnels," *NASA CR-2920*, November 1977.

[15]Cliff, Susan E., Durston, Donald A., Elmiligui, Alaa A., Walker, Eric L., and Carter, Melissa B., "Experimental and Computational Sonic Boom Assessment of Lockheed-Martin N+2 Low Boom Models," *NASA/TP-2015–218483*, January 2015.

[16]Durston, Donald A., Elmiligui, Alaa A., Cliff, Susan E., Winski, Courtney S., Carter, Melissa B., and Walker, Eric L., Experimental and Computational Sonic Boom Assessment of Boeing N+2 Low Boom Models," *NASA/TP-2015–218482,* January 2015.

[17]Cliff, S., Elmiligui, A., Aftosmis, A., Thomas, S., Morgenstern, J., and Durston, D., "Design and Evaluation of a Pressure Rail for Sonic Boom Measurements in Wind Tunnels," Seventh International Conference on Computational Fluid Dynamics (ICCFD7), ICCFD-2006, Big Island, HI, July 2012.

[18]Heineck, J.T., Retroreflective Focusing Schlieren System, US Patent 5,515,158; 1996.

[19]Weinstein, Leonard M., "Large-Field High-Brightness Focusing Schlieren System," *AIAA Journal, Vol. 31, No. 7,* July 1993.

[20]Kiris, Cetin C., Barad, Michael F., Housman, Jeffrey A., Sozer, Emre, Brehm, Christoph, and Moni-Yeta, Shayan, "The LAVA Computational Fluid Dynamics Solver," *AIAA 2014-0070,* 52nd Aerospace Sciences Meeting, January 2014.

[21]Chan, W. M., "Developments in Strategies and Software Tools for Overset Structured Grid Generation and Connectivity," *AIAA Paper 2011-3051,* 20th AIAA Computational Fluid Dynamics Conference, Honolulu, Hawaii, June, 2011.

[22]Chan, W. M., "The OVERGRID Interface for Computational Simulations on Overset Grids," *AIAA Paper 2002-3188,* 32nd AIAA Fluid DynamicsConference, St. Louis, Missouri, June, 2002.

[23]www.cd-adapco.com/products/star-ccm

[24]Cliff, S. E., Elmiligui, A. A., Campbell, R. L., and Thomas, S. D., "Evaluation of Refined Tetrahedral Meshes with Mach Cone Aligned Prisms for Sonic Boom Analysis", *Journal of Aircraft, Vol. 50 No. 3 (2013), pp. 778-790. [DOI 10.2514/1.C031943]*

[25]Housman, Jeffrey A., Sozer, Emre, and Kiris, Cetin C., "LAVA Simulations for the First AIAA Sonic Boom Prediction Workshop," *AIAA 2014-2008,* 32nd AIAA Applied Aerodynamics Conference, Atlanta, GA, June 2014.

[26]www.beta-cae.com/ansa.htm

[27]Cliff, S.E., "On the Design and Analysis of Low Sonic Boom Configurations" NASA Conference Publication 10133, High Speed Research: Sonic Boom volumes I and II Presented at the High Speed Research Sonic Boom Workshop, Ames Research Center, May 12-14, 1993.

[28]Waithe, Kenrick, "Design of a Wind Tunnel Mount for a Low Boom Test (Invited)," *AIAA 2011-3334,* 29th AIAA Applied Aerodynamics Conference, Honolulu HI, June 2011.

[29]Carlson, Harry W, Mack, Robert M., and Morris, Odell A., "A Wind-Tunnel Investigation of the Effect of Body Shape on Sonic-Boom Pressure Distributions," *NASA TN D-3106,* November 1965.

[30]Carlson, Harry W., "The Lower Bound of Attainable Sonic-Boom Overpressure and Design Methods of Approaching this Limit," *NASA TN D-1494,* 1962.

[31]Ordaz, Irian, Wintzer, Mathias, Rallabhandi, Sriram K., "Full-Carpet Design of a Low-Boom Demonstrator Concept," *AIAA 2015-2261,* 33rd AIAA Applied Aerodynamics Conference, Dallas TX, June 2015.

[32]Pearl, Jason M., Carter, Melissa B, Elmiligui, Alaa A., Winski, Courtney S., Nayani, Sudheer N., "Numerical Examination of Shock Generator Geometries and Nozzle Plume Effects on Pressure Signature," *AIAA 2016- (to be presented),* 54th AIAA Aerospace Sciences Meeting, San Diego, CA, January 2016.